Journal of Energy Storage 74 (2023) 109278

Contents lists available at ScienceDirect

Journal of Energy Storage

journal homepage: www.elsevier.com/locate/est

Research papers

Transient cooling of a lithium-ion battery module during high-performance driving cycles using distributed pipes - A numerical investigation

Jalal Jahanpanah [a], Peyman Soleymani [a], Nader Karimi [b], Meisam Babaie [c,*], Seifolah Saedodin [a]

[a] Faculty of mechanical engineering, Semnan University, Semnan, Iran
[b] School of Engineering and Material Science, Queen Mary University of London, London E1 4NS, UK
[c] School of Mechanical Engineering, University of Leeds, Leeds LS2 9JT, UK

ARTICLE INFO

Keywords:
BTMS
Time-dependent thermal management
Lithium-ion battery
Driving cycle

ABSTRACT

Transient effects are often excluded from the design and analysis of battery thermal management systems (BTMS). However, electric vehicles are subjected to significant dynamic loads causing transient battery heating that is not encountered in a steady state. To evaluate the significance of such effects, this paper presents a time-dependent analysis of the battery cooling process, based on an existing cooling system that satisfactorily operates in steady conditions. To resemble realistic conditions, the temporal variations in the battery power withdrawal are inferred from different standard driving cycles. Computational fluid dynamics is then utilized to predict the coolant and battery temperatures inside a battery module for a period of 900 s. It is shown that, for air cooling, the batteries temperature can exceed the safe limit. For example, in a high-performance driving cycle, after 200 s, the battery temperature goes beyond the critical value of 308 K. Nonetheless, the temperatures are always within the safe region when liquid is used to cool the battery module. Also, during a high-performance cycle where the flow rate is 1.230 g/s, the battery temperature decreased below the critical threshold and reached 304 K. In addition, to maintain the temperature of the batteries below the critical threshold during NYCC traffic and US06 driving cycles, a maximum coolant pressure inlet of 1.52 and 0.848 g/s, equivalent to 100 Pa and 50 Pa, respectively, are required. The temporal changes in Nusselt number distribution over the battery module, induced by the acceleration of the vehicle during the driving cycles, are also discussed. It is concluded that the assumption of a steady state might lead to the non-optimal design of BTMSs.

1. Introduction

In 2020, the transportation sector was responsible for 24 % of the direct carbon dioxide emissions worldwide [1,2], and this figure is expected to rise to 50 % by 2035 if the current trend continues [1,3]. This along with the ongoing energy crises has accelerated the efforts for further development of electric vehicles (EV) [4]. Adopting of electric vehicles, can combat the adverse effects of greenhouse gas emissions on the environment and public health but if their charging is supported by renewables energy [5]. For example, wind turbines with optimal design can be used for producing green renewable electricity [6,7]. Multi-energy complementary system such as "wind power-pumped storage-hydrogen energy storage" [8], integrated wind and photovoltaic (PV) systems [9] and marine pumped hydroelectric storage (MPHS) [10] can also be employed for more efficient renewable energy production and storage.

Lithium-ion batteries offer the most suitable cell chemistries by their high specific energy and power densities, high nominal voltage, low self-discharge rate, and long cycle life [11]. Nevertheless, Li-ion batteries, suffer from an unavoidable problem regarding large rates of heat generation, which lead to a significant increase in the batteries temperature and may even cause an explosion [12]. The consideration of battery cooling's impact in automotive, renewable, and energy storage systems is vital and should not be overlooked. Thus, Xiuxing Yin et al. [13] conducted an analysis of the influence of mechanical braking on the mooring dynamics of offshore floating wind turbines during emergencies. They highlighted the effectiveness of incorporating battery packs with both safety features and cooling mechanisms.

In automotive applications, to ensure the reliability and safety of the Li-ion batteries in EVs, the battery temperature should be preserved in a narrow safe range, somewhere between 25 to 40 °C, while the highest temperature difference in battery modules should remain under 5 °C [14]. Heat accumulation by exothermic phenomena is a critical issue

* Corresponding author.
E-mail address: m.babaie@leeds.ac.uk (M. Babaie).

https://doi.org/10.1016/j.est.2023.109278
Received 29 January 2023; Received in revised form 12 August 2023; Accepted 9 October 2023
Available online 31 October 2023

Nomenclature

A	Heat generation polynomial constants
B	Inlet fluid velocity and pressure polynomial constants
C_1	Model constant
C_2	Model constant
C_3	Model constant
C_p	Specific heat at constant pressure
C_f	Specific heat capacity of the working fluid
G_k	Generation of turbulence kinetic energy due to the mean velocity gradients
G_b	Generation of turbulence kinetic energy due to buoyancy
j	volumetric transfer current density (A)
j_{ECh}	volumetric current transfer rate due to electrochemical reaction (A)
j_{short}	volumetric current transfer rate during internal short circuit (A)
$\dot{m}$	Mass flow rate (kg/s)
Nu	Nusselt number
P	Pressure (Pa)
P	Power output mechanical (W)
Q	Heat transfer rate (W)
$Q_{nominal}$	Battery capacity in Ampere hours (Ah)
Q_{ref}	Battery capacity used in the reference (Ah)
$\dot{q}_{ECh}$	Electrochemical volumetric heat source due to electrochemical reaction (J)
$\dot{q}_{short}$	Electrochemical volumetric heat source during internal short circuit (J)
S_k	User-defined source terms
S_ε	User-defined source terms
T	Temperature (°C/K)
t	Time (S)
U	NTGK model parameter (V)
V	Voltage (V)
Y	NTGK model parameters (S/m^2)

Greek symbols

∇	Gradient operator
ρ_f	Density of the working fluid [kg·m^{-3}]
ϑ_f	Kinematic viscosity of the fluid [m^2·s^{-1}]
σ_+	electric conductivities for the positive electrodes (1/Ω)
σ_-	electric conductivities for the negative electrodes (1/Ω)
Φ_+	phase potentials for the positive electrodes (V)
Φ_-	phase potentials for the negative electrodes (V)
ν	kinematic fluid viscosity (m^2/s)
ε	Turbulent dissipation rate (m^2/s^3)
σ_k	Turbulent Prandtl numbers for k
ε_k	turbulent Prandtl numbers for ε

Acronyms

BTMS	Battery thermal management system
C-rate	Current charge/discharge rate
CFD	Computational fluid dynamic
DoD	Battery depth of discharge
EV	Electrical vehicle
MSMD	Multi-Scale Mutli-Domani
NTGK	Newman, Tiedemann, Gu, and Kim model

that can adversely affect the battery performance, lifetime, and safety. The subsequent temperature rise due to the electrochemical response of lithium batteries can overheat the batteries [15,16]. In addition, during the battery discharging, lithium-ion batteries generate a considerable quantity of heat [17,18]. Most importantly, the heat release in the battery could be strongly time-dependent, which challenges the battery thermal management system (BTMS) [19,20].

In general, depending on the need for any external power source, battery cooling is divided into two categories passive and active systems. In the active process, cooling is provided by circulating air, water, or other coolants [21]. In the passive process, heat transfer is conducted through conduction, free convection, and radiation without any external source of power [22]. Air cooling is an optimal cooling method due to its low manufacturing costs and simple configuration. However, it suffers from the low heat capacity and thermal conductivity of air [23–25]. Liquid cooling is, generally, more effective than air cooling mainly due to the higher specific heat capacity of liquids compared to that of air [26]. Developing a properly BTMS liquid-cooled BTMS often includes two approaches direct and indirect contact. The design of direct contact BTMS needs the details of batteries' electrical, electrochemical, and thermal behaviors. In particular, an in-depth understanding of the dynamics of heat generation, thermal transport, and heat dissipation processes is required [27,28].

In recent years, many researchers investigated liquid and air cooling for BTMS, see for example [27,29–32]. In a new cooling strategy for an air-cooled battery pack with lithium-ion pouch cells in a hybrid electric vehicle, three orifices were constituted in each of the sidewalls of the outlet duct [33]. The orifices could reduce the maximum temperature of the cells across the pack by about 1.1 °C, and the maximum lumped peak cell temperature in the pack was reduced by approximately 8.0 °C. In addition, the total pressure drop of the battery pack was minimized to about 43 % less than that of the baseline battery pack [33]. Further, a novel liquid coolant-based thermal management system for an 18650 battery pack showed that thermal management effectively cools down the pack even at lower coolant flow rates [34]. For the higher discharge rates and low coolant flow rates, the maximum temperature gradient was maintained within 7 K [34].

As the operation of a vehicle (and thus the discharge rate) is often unsteady, time-dependent thermal management is an essential issue for battery thermal management [35–37]. However, most existing studies on battery cooling assumed steady conditions [30–32]. Only a limited number of investigations have been conducted on the heat transfer characteristic of batteries under the dynamic loads set by unsteady charge and discharge [35,38]. In an experimental attempt to prevent over-cooling phenomena, a controllable cooling system based on forced air cooling was analyzed [35]. The cooling system turns on when the battery temperature reaches a critical number, and it switches off when the battery pack temperature returns to the safe zone. This study showed that, compared to steady systems, the unsteady cooling system could offer a 30 % reduction in energy consumption of the cooling system [35]. Additionally, a staggered-arranged battery pack was considered to investigate the effect of natural and forced air cooling. The result showed that natural air-cooling was suitable for 0.5C of current, but for 1C and higher current intensity, they recommend a forced air-cooling system with 0.8 m/s air inlet velocity. Also, it was reported that a forced air cooling system could extend the lifetime of Li-ion batteries by about two months for every degree of temperature enhancement in the optimal temperature range of 20 °C to 40 °C [39,40]. Recently, Saeed et al. [41], examined the dynamic response of a battery pack to harmonic disturbances imposed over the internal heat generation of the batteries. These authors argued that any arbitrary temporal disturbance could be decomposed into several harmonic disturbances through the application of Fourier transformation. They showed that for low amplitude and short wavelength disturbances, the battery thermal response could remain linear, which implies the applicability of linear control strategies [41,42].

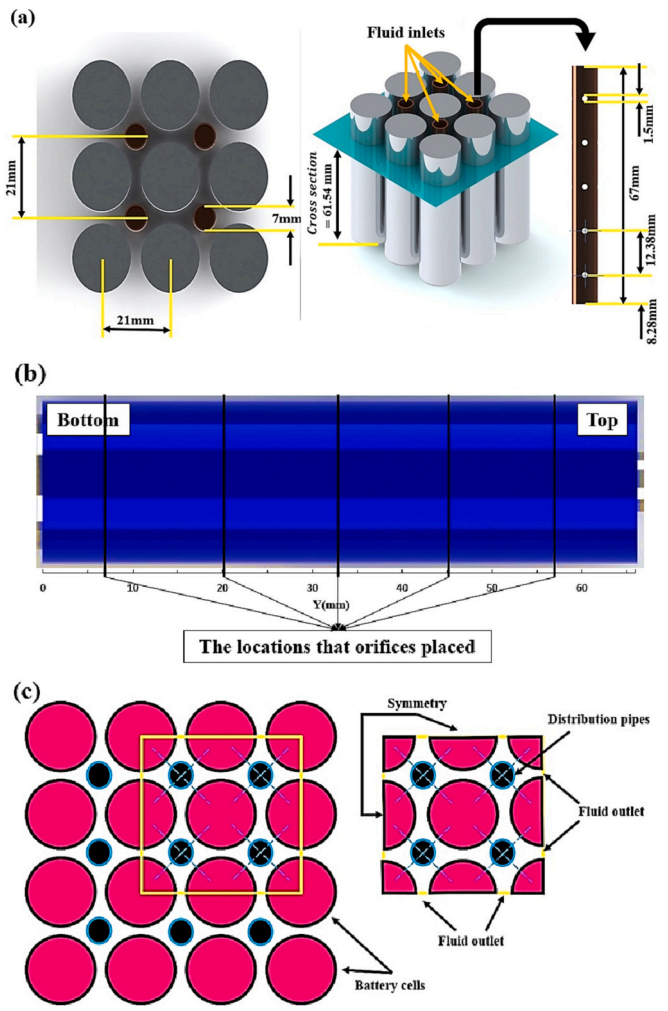

Fig. 1. Schematic of the (a) cylindrical batteries and water/air distribution pipes positions with the orifices (b) The location where cooling fluid contacts with the battery surface through orifices (c) computational domain.

In reality, the dynamics of battery heat generation are dominated by variations in the speed and power demand of the vehicle, which can be analyzed during standard driving cycles. Hence, simulation of the thermal response of batteries to the power variations induced by driving cycles could be a good indication of the time-dependent thermal behavior of the battery pack. In an early attempt, battery operation was treated as a heat source using a simple thermal model, and simulations were carried out for two electric vehicle drive cycles [43]. They found that a significant temperature enhancement arises during the severe drive cycle, and practical temperature control is needed to maintain optimal cell performance [43]. To evaluate the thermal performance, the thermal profiles from a 30 Ah prismatic cell were simulated for a complete US06 driving cycle. The results indicated that the US06 drive cycle average current demand was 0.56C over 50 km [44]. In addition, the drive cycle data were employed to find the optimal design performance under realistic driving conditions. Hence, the current and voltage profile transients for a 600 s-long US06 drive cycle with aggressive driving behavior were analyzed. The results revealed that even at an excessive temperature of 40 °C with high charge or discharge currents, the suggested liquid cooling system allowed the battery temperature to achieve the pre-set standard in 600 s [45].

The review of the literature shows that the evaluation of the performance of BTMS under unsteady conditions has received very limited attention. To address this gap, the current research aims to examine the time-dependent thermal performance of a 18650 Li-ion battery module with fluid distribution pipes and five orifices embedded among the batteries for uniformly distribution of the fluid on the outer surface of the batteries. To achieve this aim, the thermal management of the battery pack will be analyzed based on different driving cycles by developing a computational model. The results of this work will contribute to exploration of the differences between steady-state and transient battery thermal response and evaluation of the BTMS designs that are developed under steady-state assumptions. Also, this study proposes a new type of cooling system that varies with the temperature of batteries in different driving cycles. In this design, air is the coolant fluid, and water is used in critical conditions. Finally, this research will demonstrate the battery temperature in different driving conditions and the optimal cooling conditions by using coolant fluid pipes for improving the battery thermal performance and extending the lifespan. This research is essential in developing more efficient and reliable battery cooling systems for electric vehicles, which can help to reduce energy consumption and increase the overall efficiency of the vehicle.

2. Model and methodology

2.1. Physical model

A typical battery pack consists of several battery modules connected to each other in parallel and in series. Every module includes several battery cells associated with particular series/parallel assortments to reach the maximum voltage and current. The numbers of battery cells and modules vary based on the different capacities and power specifications of the electric vehicle [46,47]. In the current investigation, a pack of 85 kWh energy storage capacity (similar to the Tesla S series) was considered.

The selected 18650 Li-ion (Li[Ni0.5Co0.2Mn0.3]O2/C), features 2 Ah current and 3.6 V voltage, with a density of 2500 $kg{\cdot}m^{-3}$, and specific heat capacity (*Cp*) of 1108 $j{\cdot}kg^{-1}\,K^{-1}$, and thermal conductivity (*K*) of 28 $W{\cdot}m^{-1}\,K^{-1}$. The selection of the battery type requires thorough consideration of various factors to fulfill the total current and voltage demands. These factors include vehicle range requirements, constraints related to vehicle weight and space, power demand, efficiency, and energy consumption considerations, as well as the cost factors. During the battery pack design process, all these aspects should be carefully evaluated and taken into account. Fig. 1 shows the schematic views of the physical and computational models of the battery module under investigation. Fig. 1 shows the dimensions and the location where cooling fluid coming out of the pipe through orifices is illustrated in Fig. 1b. To reduce the computational burden, a symmetric unit, shown in Fig. 1c, was employed as the computational domain.

As depicted in Fig. 1, for the coolant distribution around the battery cells, a pipe distribution with five orifices with diameters of 1.5 mm was selected. These are similar to that presented by Zhou et al. [48] and could distribute the coolant throughout the batteries wall to reduce the temperature uniformly. The pipe distribution with five orifices and a diameter of 1.5 mm showed the best cooling performance according to the results in [48]. Therefore, the fluid flow enters the top section of the pipes and flow though the orifices with a higher velocity, while pipe ends are closed.

The cooling methodology examined in the current investigation is noteworthy for its high level of optimization. However, it was observed that while effective under steady-state conditions, the cooling approach was inadequate in extreme situations possibly encountered during driving cycles. To tackle this challenge, a dynamic cooling system was integrated into the design, which can adapt the inlet coolant fluid in response to variations in the battery's temperature and power demands. Moreover, to identify all potential extreme situations during driving cycles, an analysis was performed to determine the optimal cooling fluid inlet velocity.

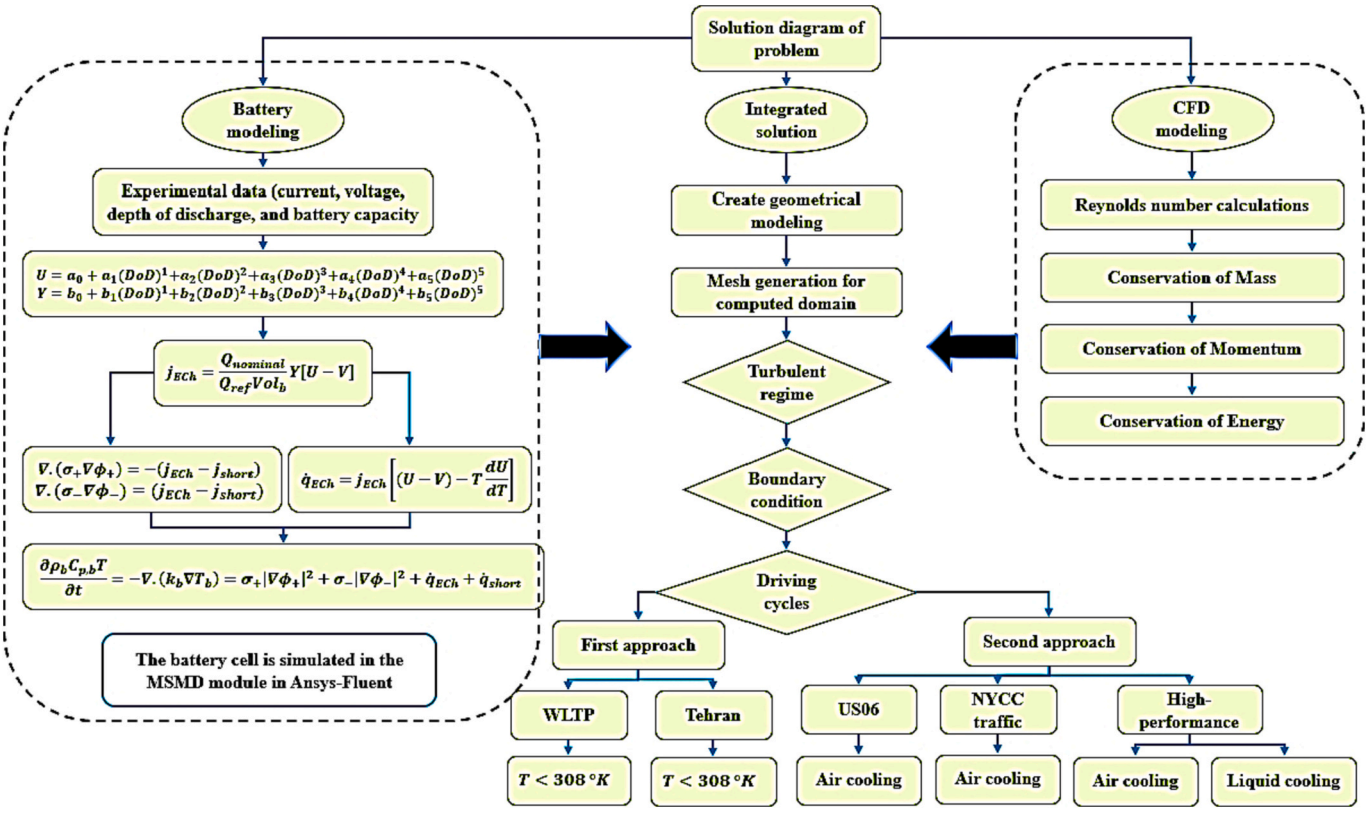

Fig. 2. The flowchart for NTGK battery modeling is integrated with CFD modeling.

2.2. Battery model

A computational model for the domain shown in Fig. 1 was developed in Multi-Scale Multi-Domain (MSMD) module in Ansys-Fluent 2020R2. The lithium-ion battery simulation is intricate due to the existence of multi-domain, multi-physics elements, and various physical length scales [49]. Utilization of a Multi-Scale Multi-Domain (MSMD) strategy offers an effective way of managing this complexity [50]. To assess the battery cooling model, a cell-level distributed model was required that could demonstrate the temperature gradient within a battery cell and its influence on the local condition of the charge. In general, two comprehensive classes of models could be used for this purpose: Continuum Models (CM) a cost-effective strategy to examine the influence of geometric structure and dimension in microscale batteries. Equivalent Circuit Models (ECM) is a battery model frequently employed in the battery management system (BMS) to monitor and control lithium-ion batteries. This phenomenological approach is widely used in BMS because of its computational advantages. [51–54]. The Newman, Tiedemann, Gu, and Kim (NTGK) model, matches ECM [55]. NTGK model is a reasonable approach to incorporate two and three-dimensional Li-ion battery simulation and to recognize thermal diffusion through electrochemical modeling. In addition, this approach considers the resistors and capacitors, allowing accurate thermal data regarding battery electrical performance. Furthermore, due to its simplicity, the ECM model has been broadly utilized in numerous circuit arrangements and control algorithms [56]. For these reasons, the NTGK

Table 1
Heat generation (A_{1-10}), and pressure inlet (B_{1-10}) coefficient New York city cycle NYCC-Traffic mode driving.

A_1	A_2	A_3	A_4	A_5	A_6	A_7	A_8	A_9	A_{10}
7.8760e+1	1.8897e+1	−9.0626e-1	2.2222e-5	−1.2450e-4	5.5301e-7	−1.4344e-9	2.1711e-12	−1.7794e-15	6.1086e-19

B_1	B_2	B_3	B_4	B_5	B_6	B_7	B_8	B_9	B_{10}
−1.3466e-1	3.7074e-2	−1.416e-3	2.2222e-5	−1.730e-7	7.5342e-10	−1.9297e-12	2.8951e-15	−2.3572e-18	8.0503e-22

Table 2
Heat generation (A_{1-10}), and pressure inlet (B_{1-10}) coefficients for US06 driving cycle.

A_1	A_2	A_3	A_4	A_5	A_6	A_7	A_8	A_9	A_{10}
4.536131e+2	−8.2084	1.2573e-1	−1.4455e-3	1.0876e-5	−5.1251e-8	1.4833e-10	−2.5475e-13	2.3749e-16	−9.2394e-20

B_1	B_2	B_3	B_4	B_5	B_6	B_7	B_8	B_9	B_{10}
3.1918	−1.1405e-1	2e-3	−1.9569e-5	1.1565e-7	−4.2930e-10	−1.4471e-15	−1.4471e-15	1.1624e-18	−3.9940e-22

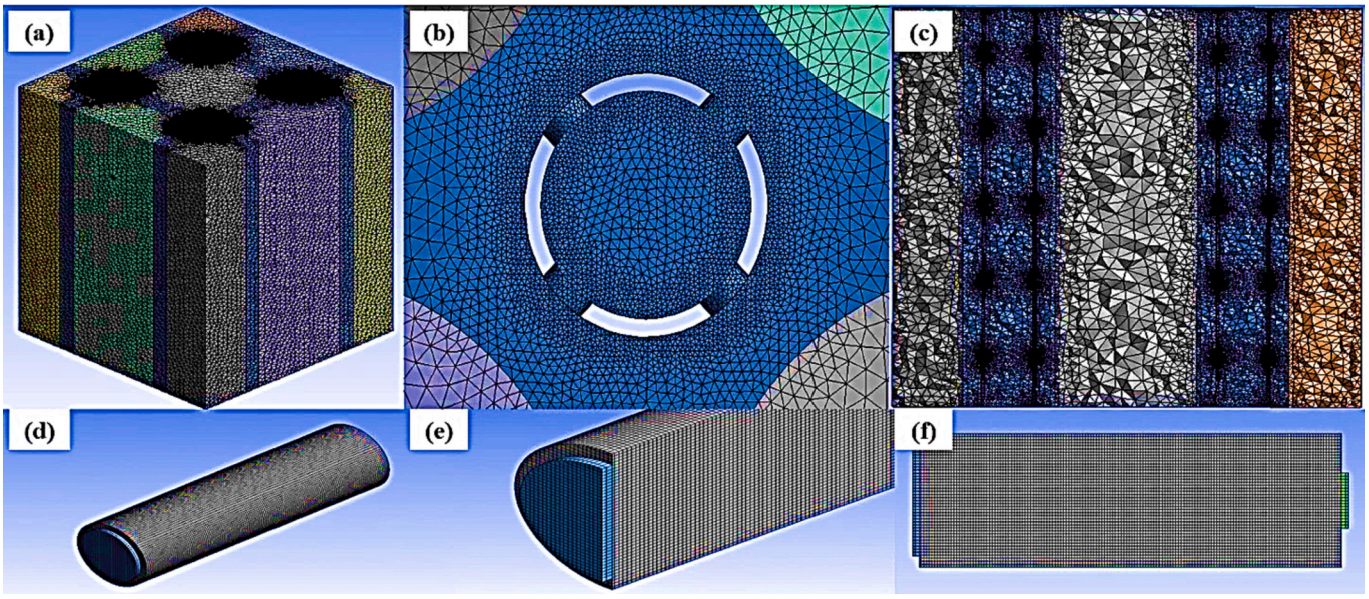

Fig. 3. The mesh structure of the models, (a) Isometric system (b) heat distribution pipe (c) Lateral view of the model (d) Single battery (e, f) lateral view of the single battery.

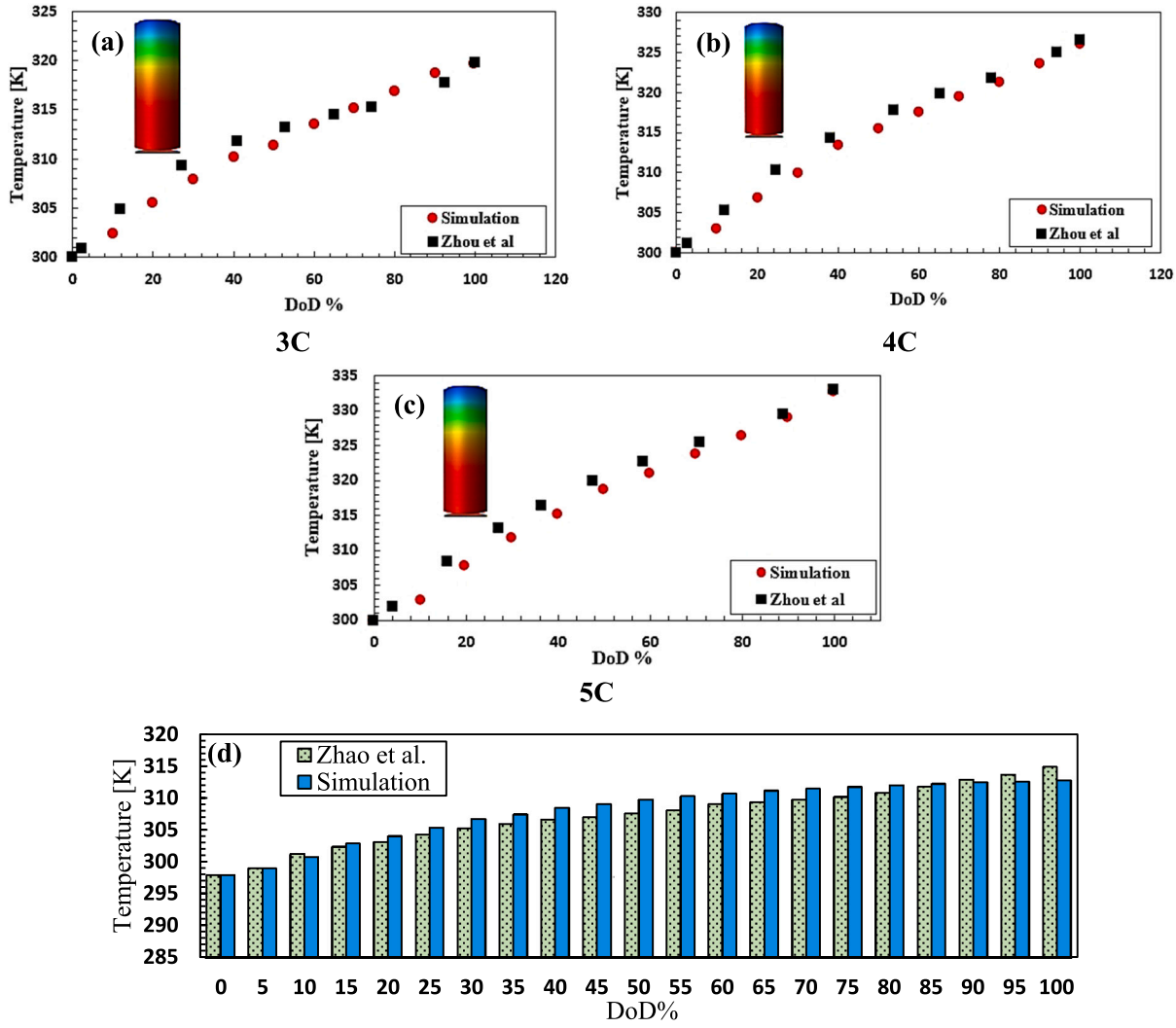

Fig. 4. Comparison between the current numerical simulations and the experiment of Zhou et al. [48] (a), (b), and (c) experimental data for different battery depths of discharge in the simulation of battery cells for different current intensities (d) validation of the numerical simulations of the computational domain.

Table 3
The total inlet mass flow rates (inlet Fig. 1a) for different driving cycles in specified points (A), (B), (C), and (D).

Driving cycles	Mass flow rate through the orifices (g/s)			
US06-air coolant	A	B	C	D
	0.808	0.32	0.544	0.848
NYCC traffic-air coolant	0.565	1.52	0.570	0.28
High performance-air coolant	2.71			
High performance-liquid coolant	1.230			

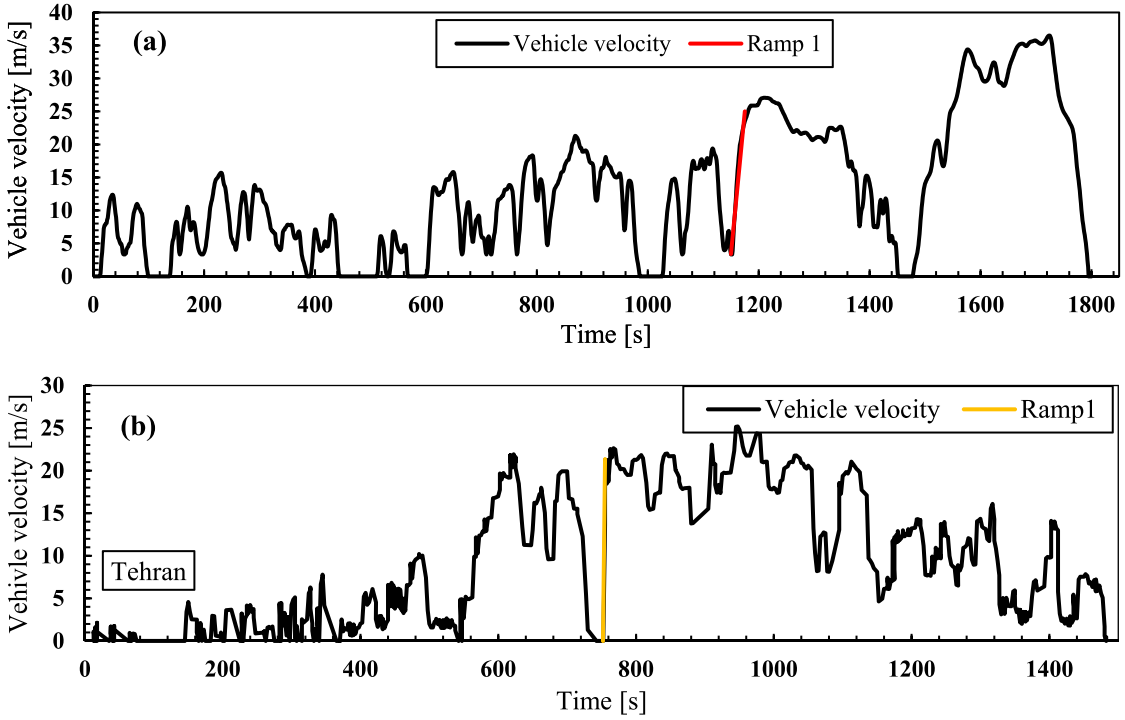

Fig. 5. (a) WLTP and (b) Tehran driving cycle, highest power requirement.

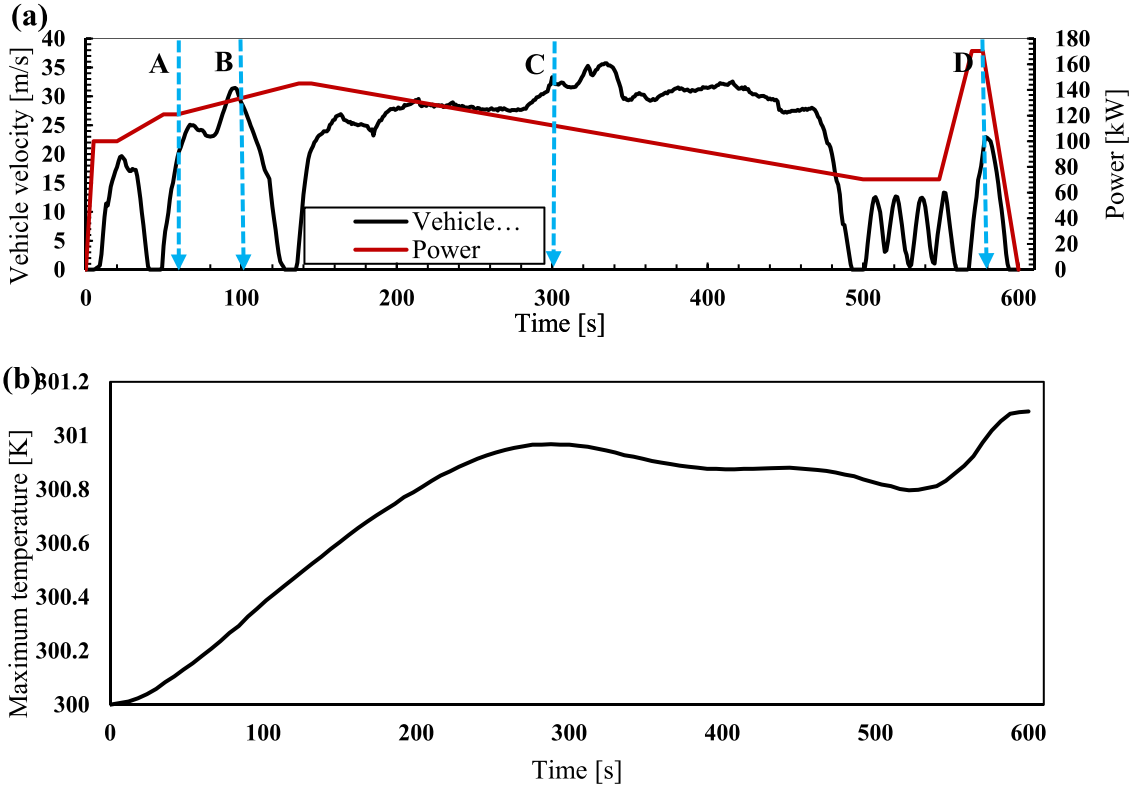

Fig. 6. (a) The US06 drive cycle vehicle's speed and conversion to the required power (b) The maximum battery temperature variations during the US06 drive cycle using air-cooling.

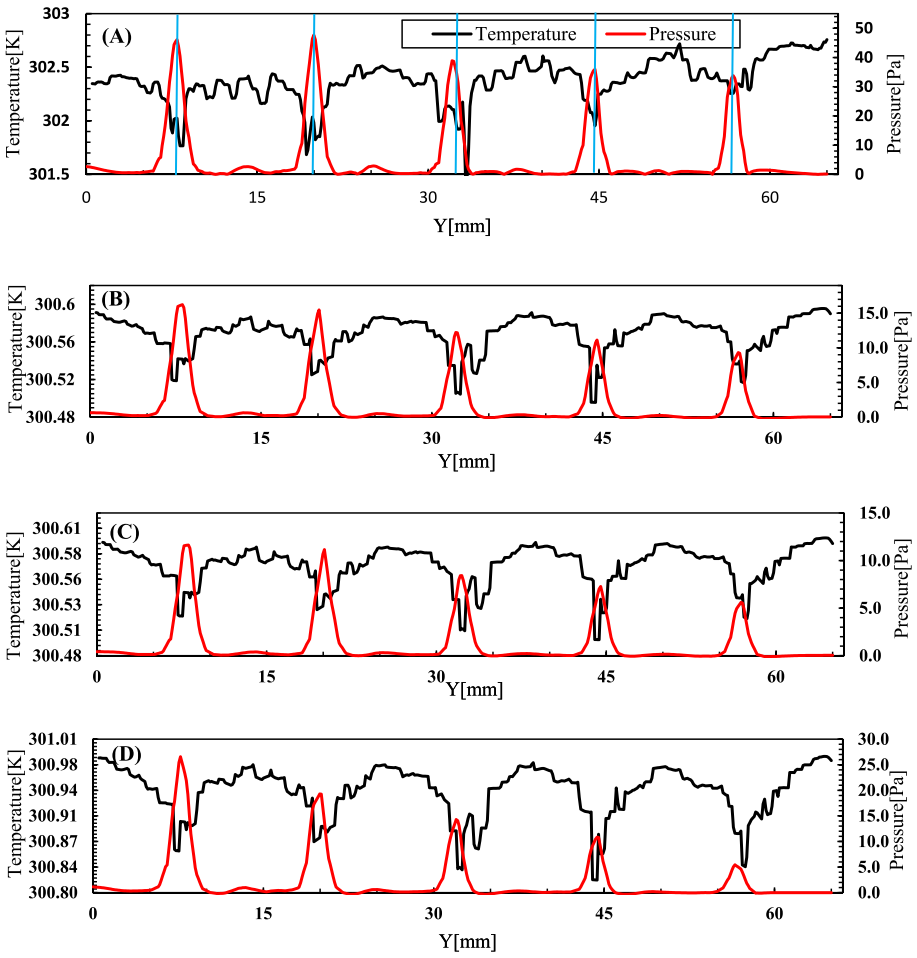

Fig. 7. Battery surface temperature variations in front of orifices, where designated in (A) with the simultaneous inlet air coolant pressure changes for the US06 drive cycle at the moments specified by A, B, C, and D in Fig. 6a.

model was employed in the current investigation.

2.2.1. Time-dependent thermal management

Overall, two different approaches were chosen to examine the battery performance in realistic time-dependent conditions. First, the maximum vehicle power demand was calculated for the steepest ramp from WLTP and Tehran driving cycles. This value then was converted into current and ultimately to heat flux, and cooling was applied for DoDs from 0 to 100 %. However, this approach may not completely represent reality because it only considers one ramp during the drive cycle, see Fig. 5. The second approach was to convert the entire driving cycle into power, electrical current, and heat flux. For this purpose, all the upward ramps were considered. Converting all the ascending ramps into heat flux and obtaining the heat flux application equation based on the time that corresponds to driving cycles. This leads to a more accurate analysis of the heat generated by the batteries during the driving cycles. Therefore, to find the heat flux equation, the heat flux was calculated for all the ascending ramps. It was verified that a tenth-degree polynomial could be fitted for the heat flux generated during the cycle. The flowchart for NTGK battery modeling integrated with CFD modeling is shown in Fig. 2. In the first approach, WLTP and Tehran driving cycles were assessed, the maximum temperature in these cycles was placed in the safe range below 308 K, and the cooling fluid was not required. However, for the second approach, the US06, NYCC traffic, and high-performance drive cycle were evaluated. Air cooling was used for all the second approach cycles, and both air and liquid cooling were assessed for the high-performance cycle.

2.2.2. Battery thermal and electrical field models

For a battery cell, the thermal distribution fields were simulated through the discretization of energy equations [57]. The conservation of thermal and electrical equations for battery thermal management systems is shown in Eq. (1) [57].

$$\frac{\partial \rho_b C_{p,b} T}{\partial t} = -\nabla\cdot(k_b \nabla T_b) = \sigma_+ |\nabla \phi_+|^2 + \sigma_- |\nabla \phi_-|^2 + \dot{q}_{ECh} + \dot{q}_{short} \quad (1)$$

Eq. (2) and Eq. (3), show the current flux at the positive and negative terminals [50].

$$\nabla\cdot(\sigma_+ \nabla \phi_+) = -(j_{ECh} - j_{short}) \quad (2)$$

$$\nabla\cdot(\sigma_- \nabla \phi_-) = (j_{ECh} - j_{short}) \quad (3)$$

It should be noted that without an internal short circuit, j_{short}, and $\dot{q}_{short}$ values were set to zero.

The current density and the depth of the discharge were calculated through the following equations Eq. (4), and Eq. (5), where the V represents cell voltage. In addition, Y and U indicate the depth of discharge functions while $Q_{nominal}$ and Q_{ref} are acquired empirically [57].

$$j_{ECh} = \frac{Q_{nominal}}{Q_{ref} Vol_b} Y[U - V] \quad (4)$$

$$DoD = \frac{Vol_b}{3600 Q_{nominal}} \int_0^t j dt \quad (5)$$

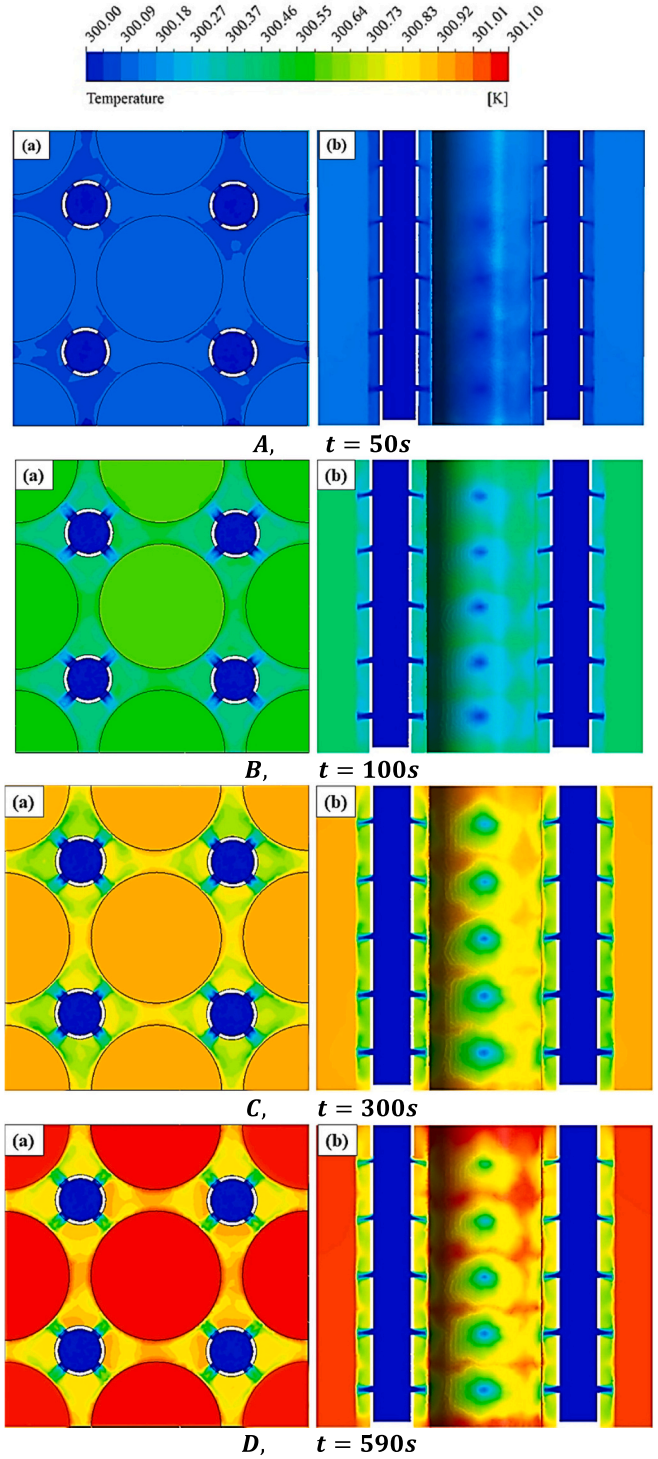

Fig. 8. The temperature variations contours through the air-cooling for the US06 drive cycle (a) top view from cross section indicated in Fig. 1a (b) side view.

Eq. (6) represents an electrochemical heat release in which the differences between U and V indicate heat generation by overpotential. The second term in brackets in Eq. (6) models the heat generation by entropic heating. Further, the parameters of U and Y in Eq. (7) and Eq. (8) are determined empirically [58–60].

$$\dot{q}_{ECh} = j_{ECh}\left[(U-V) - T\frac{dU}{dT}\right] \tag{6}$$

$$U = a_0 + a_1(DoD)^1 + a_2(DoD)^2 + a_3(DoD)^3 + a_4(DoD)^4 + a_5(DoD)^5 \tag{7}$$

$$Y = b_0 + b_1(DoD)^1 + b_2(DoD)^2 + b_3(DoD)^3 + b_4(DoD)^4 + b_5(DoD)^5 \tag{8}$$

2.3. Transient polynomial expressions

The standard velocity-time driving cycles were converted to mechanical power output for the transient simulation of driving cycles. Eq. (9) expresses the estimation of EVs mechanical power. The total battery pack current can be approximated by Eq. (9). Then, by converting it to battery cell current and discharge rate, the heat flux was calculated by using the MSMD modules in Ansys-Fluent. A ten-degree polynomial, Eq. (10), was considered for predicting the heat flux fluctuating changes during the driving cycles with the EV's velocity changes. In Eqs. (10) and (11), A and B are constant coefficients and X represents time [42].

$$F = ma \Rightarrow \overset{\times v}{\underbrace{F\cdot v}}_{P} = ma\cdot v \Longrightarrow \begin{cases} P = ma\cdot v \\ P = I \times V \end{cases} \tag{9}$$

$$\dot{Q}_{gen} = \sum_{i=1}^{10} A_i X^i \tag{10}$$

As already stated, one of the critical factors in improving the performance of battery thermal management is the inlet velocity and pressure of the coolant flows. For thermal management, it is necessary to know the current output from the batteries. By estimating the battery discharge rate, the developed heat flux could be obtained. Here, the first mechanical power based on driving cycles was approximated. This was subsequently converted to the discharge rate for the analysis of heat flux changes during the driving cycles through the MSMD module in Ansys-Fluent. Next, the inlet cooling fluid pressure and velocity were analyzed to achieve the optimum inlet pressure and velocity corresponding to mechanical power changes during the driving cycles. A ten-degree polynomial by Eq. (11) was considered for simulating the time-dependent variations of the inlet pressure (inlets in Fig. 1a) [42].

$$P_{inlet} = \sum_{i=1}^{10} B_i X^i \tag{11}$$

Polynomial coefficients for heat generation and pressure inlet expressions are listed in Tables 1 and 2. for the New York City Cycle Traffic (NYCC-Traffic mode) and a high acceleration aggressive driving cycle (US06) or the supplemental FTP driving cycles.

2.4. Governing equations of fluid flow and numerical scheme

The Reynolds Average Navier-Stokes approach was taken, and the eddy viscosity concept derived from the Boussinesq approximation was employed. The Realizable k- ε was applied as the turbulence model due to the proper convergence. The standard wall function was employed to solve the governing equations near the battery walls. In addition, the Realizable k- ε turbulence model reasonably resolves the near-wall turbulent flows [61]. The following partial differential equations express the equations of continuity and conservations of momentum and energy. It is worth noting that the Richardson number was calculated to be 0.0033, and therefore mixed convection effects were ignored.

The flow governing equations are as follows.

Continuity equation [62]:

$$\frac{\partial \rho_f}{\partial t} + \frac{\partial}{\partial x_i}\left(\rho_f u_i\right) = 0 \tag{12}$$

Momentum equation [63]:

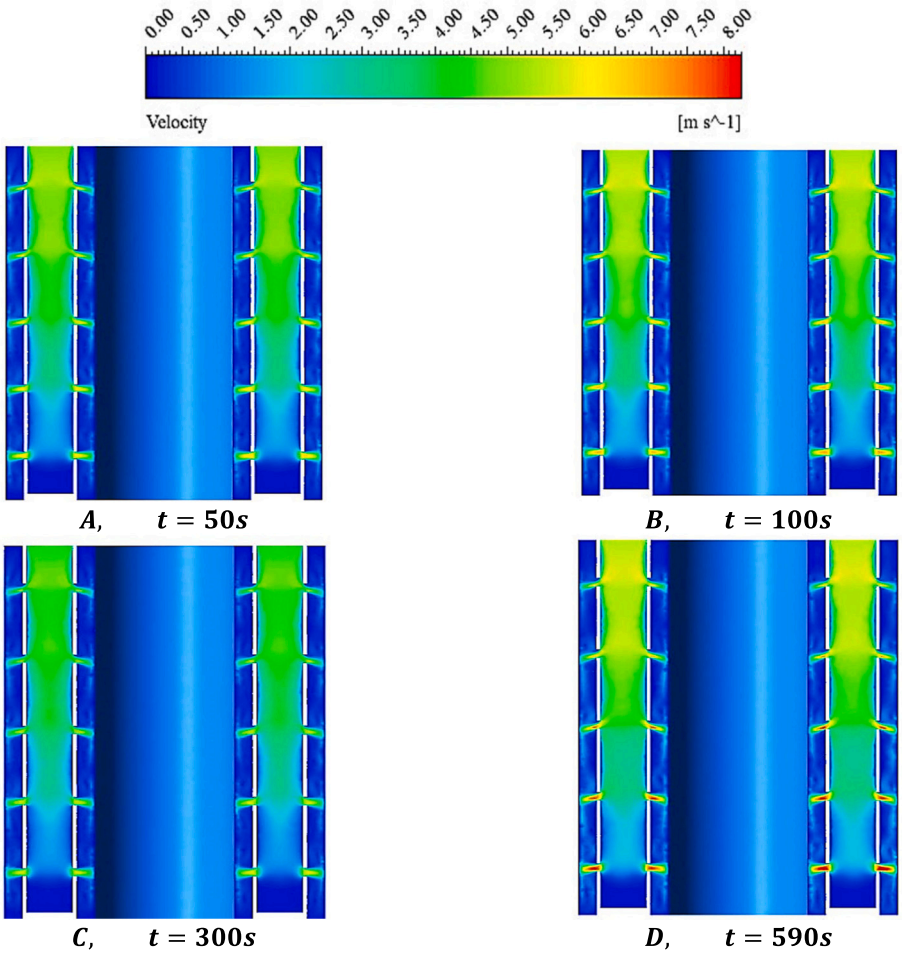

Fig. 9. The fluid velocity contours for A, B, C, and D in Fig. 6a by air-cooling in the US06 drive cycle.

$$\frac{\partial}{\partial t}(\rho u_i)+\frac{\partial}{\partial x_j}(\rho u_i u_j)=-\frac{\partial p}{\partial x_i}+\frac{\partial}{\partial x_j}\left[\mu\left(\frac{\partial u_i}{\partial x_j}+\frac{\partial u_j}{\partial x_i}-\frac{2}{3}\delta_{ij}\frac{\partial u_i}{\partial x_j}\right)\right]+i\frac{\partial}{\partial x_j}\left(-\rho_f\overline{u_i'u_j'}\right) \tag{13}$$

where $-\rho\overline{u_i'u_j'}$ represents the Reynolds stress tensor and was defined as follows:

$$-\rho_f\overline{u_i'u_j'}=\mu_t\left(\frac{\partial u_i}{\partial x_j}+\frac{\partial u_j}{\partial x_i}\right)-\frac{2}{3}\left(\rho_f k+\mu_t\frac{\partial u_i}{\partial x_j}\right)\delta_{ij} \tag{14}$$

Energy equation [64]:

The conservation of energy for the working fluid is shown in Eq. (15).

$$\rho_f C_{p,f}\frac{\partial T_f}{\partial t}+\nabla\left(\rho_f C_{p,f}\vartheta_f T_f\right)=\nabla\cdot\left(k_f\nabla T_f\right) \tag{15}$$

where the $C_{p,f}$ is the specific heat of the fluid, T_f is the temperature of the fluid, and k_f represents of thermal conductivity of the fluid.

The $k-\varepsilon$ *turbulence* model equations [65]:

$$\frac{\partial}{\partial t}\left(\rho_f k_f\right)+\frac{\partial}{\partial x_i}\left(\rho_f k u_i\right)=\frac{\partial}{\partial x_j}\left[\left(\mu+\frac{\mu_t}{\sigma_k}\right)\frac{\partial k_f}{\partial x_j}\right]+G_k+G_b-\rho_f\varepsilon-Y_M+S_k \tag{16}$$

$$\frac{\partial}{\partial t}\left(\rho_f\varepsilon\right)+\frac{\partial}{\partial x_j}\left(\rho_f\varepsilon u_j\right)=\frac{\partial}{\partial x_i}\left[\left(\mu+\frac{\mu_t}{\sigma_\varepsilon}\right)\frac{\partial\varepsilon}{\partial x_j}\right]+\rho_f C_1 S\varepsilon-\rho_f C_2\frac{\varepsilon^2}{k+\sqrt{\nu\varepsilon}}+C_{1\varepsilon}\frac{\varepsilon}{k}C_{3\varepsilon}G_b+S_\varepsilon \tag{17}$$

The realizable k- ε turbulence model constants were considered as follows: $C2-\varepsilon=1.9$, TKE Prantdl number = 1, TDR Prantdl number = 1.2, energy Prantdl number = 0.85, and wall Prantdl number = 0.85 [66]. The Nusselt number for forced fluid convection through the air orifices was calculated using the following equation.

$$Nu=\frac{hD}{k} \tag{18}$$

where h is the convective heat transfer coefficient (W/m^{2}K), D is the battery cell diameter (m), and k is the thermal conductivity of the fluid (W/mK).

Eqs. (12)–(17) were solved numerically. A second-order upwind approach was used for the lower convergence rates, while the SIMPLEC algorithm was employed for the coupling of pressure and velocity. The standard wall function was determined to solve the near-wall turbulence function in the wall function approach. As mentioned before, for the battery simulations, to calculate the battery heat flux in different operational rates based on driving cycles, the MSMD module was activated. All the investigations were carried out by utilizing Green-Gauss node-based approach. The computation continued until the residuals of all equations were less than 10^{-6}.

3. Mesh Independence study

Fig. 3 presents a grid independence analysis for the battery cell and the computational domain of the battery pack [67]. Unstructured and structured meshes were generated by ANSYS Meshing for the computational domain of the battery pack and battery cell. Near-wall boundary

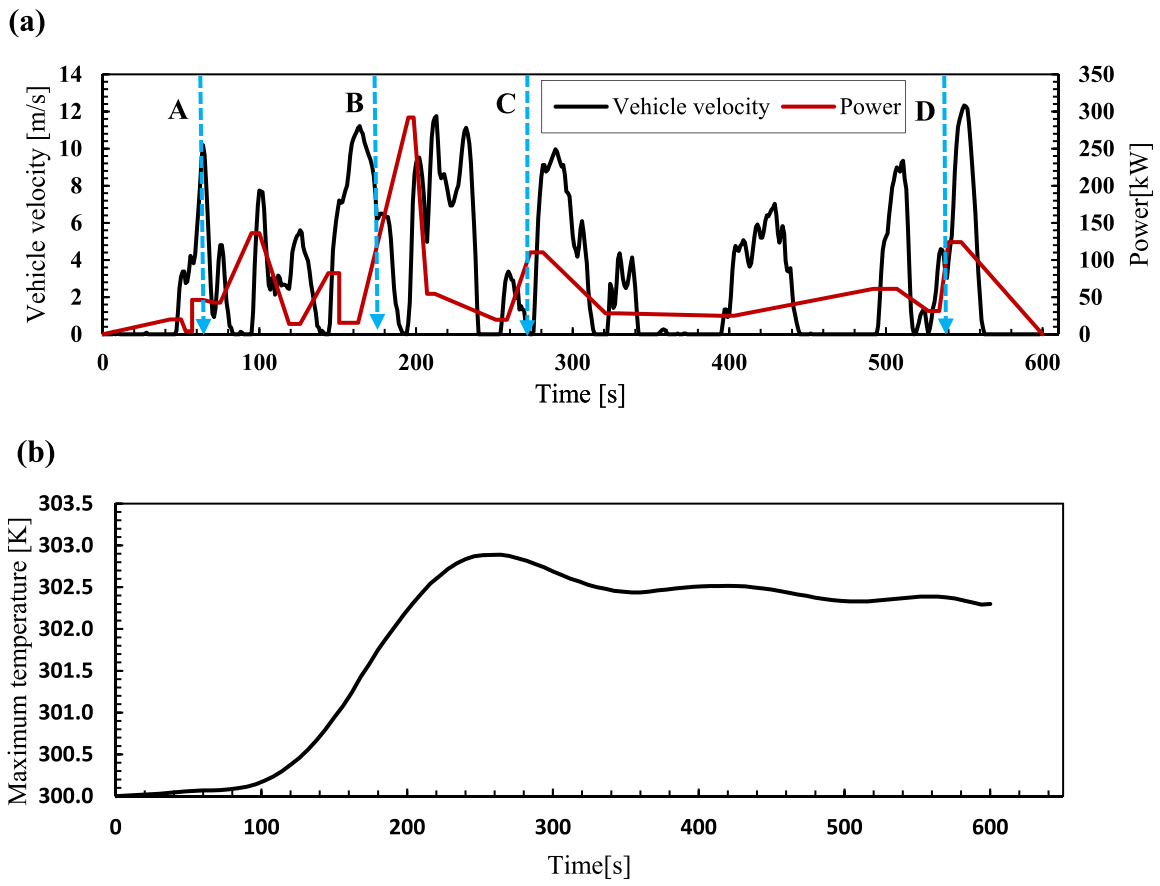

Fig. 10. (a) NYCC-traffic drive cycles converted to the required power (b) The maximum battery temperature variations during the drive using the air-cooling.

pressure, velocity fluctuations, and temperature gradient were improved by controlling all parameters in those parts. Grid independency tests were carried out by analyzing the maximum temperature of the batteries. Different mesh sizes (1867845, 2428126, 3156648, and 4419309 elements) were evaluated based on 4C, while the maximum temperature of the batteries was the same (326 K) with a minor difference in 3156648 and 4419309 elements. Hence, a grid with 3156648 cells was selected for reducing the computational burden. Further, the average orthogonality number was between 0.8 and 0.9, implying that the mesh quality was reasonable.

4. Validation of the numerical simulations

In order to validate the current numerical investigation, the maximum temperature of the battery cell in three different discharge rates of 3C, 4C, and 5C was evaluated. One battery cell was simulated for different discharge rates and a comparison was made with the experimental data of Zhou et al. [48] as shown in Fig. 4. In this figure, the maximum temperature of the battery cell was simulated by considering electro-chemistry, Ohmic or Joule heating, reversible entropic heating, and contact resistance inside the battery cell. The temperature along the battery cell rises as the depth of discharge (DoD) goes up. DoD is the percentage of discharged battery to the battery's total capacity [68]. As can be seen, the battery's temperature around the positive terminal is higher than that near the negative terminal in the case of the steady discharge rate. Based on the numerical results, the maximum error for the simulation of the battery cell was achieved at 3C with a value of 2.58 %. Fig. 4b compares the current simulation data with the experimental data of Zhou et al. [48] for different values of DoD. This shows that the maximum and average differences are 9.8 % and 5.3 %, respectively, at 55 % DoD.

The total mass flow rates studied in transient simulations for different driving cycles are listed in Table 3. These values represent the summations inlet mass flow rate in specified points of (A), (B), (C), and (D) in Figs. 6a, 10a, 14, and 18. In high-performance air and liquid cooling, there were no particular fluctuations in flow rate in the specified points as there were no vehicle speed fluctuations. Hence, battery temperature over the drive cycle increased monotonically. The mass flow rates were, therefore, considered constant because the fluid inlets (Fig. 1a) were constant.

5. Results and discussion

The required mechanical power can be approximated by Eq. (9) for the EVs using the vehicle's weight and acceleration during the driving cycle. Further, by ignoring conversion losses, mechanical power is assumed to be equivalent to electrical power, which facilitates the calculation of the current withdrawal from the battery. Hence, the heat flux values for the battery cells are calculated by converting the mechanical power to current and then simulating batteries based on the discharge rate. Then, by including those in the final simulation as constant heat flux in the battery module, the time-dependent temperature changes of the batteries are obtained [69].

Fig. 5 shows the World-harmonized Light-duty vehicles Test Procedure (WLTP), a globally coordinated standard test used for pollutants, CO_2 emissions, and fuel consumption of conventional, hybrid, and electric vehicles, and Tehran driving cycles. Based on the first approach (see Section 2.2.1), the most significant power demand occurs when the vehicle's speed increases with a sharp inclination during the driving cycles. Fig. 5a shows the highest power requirement for EVs happening

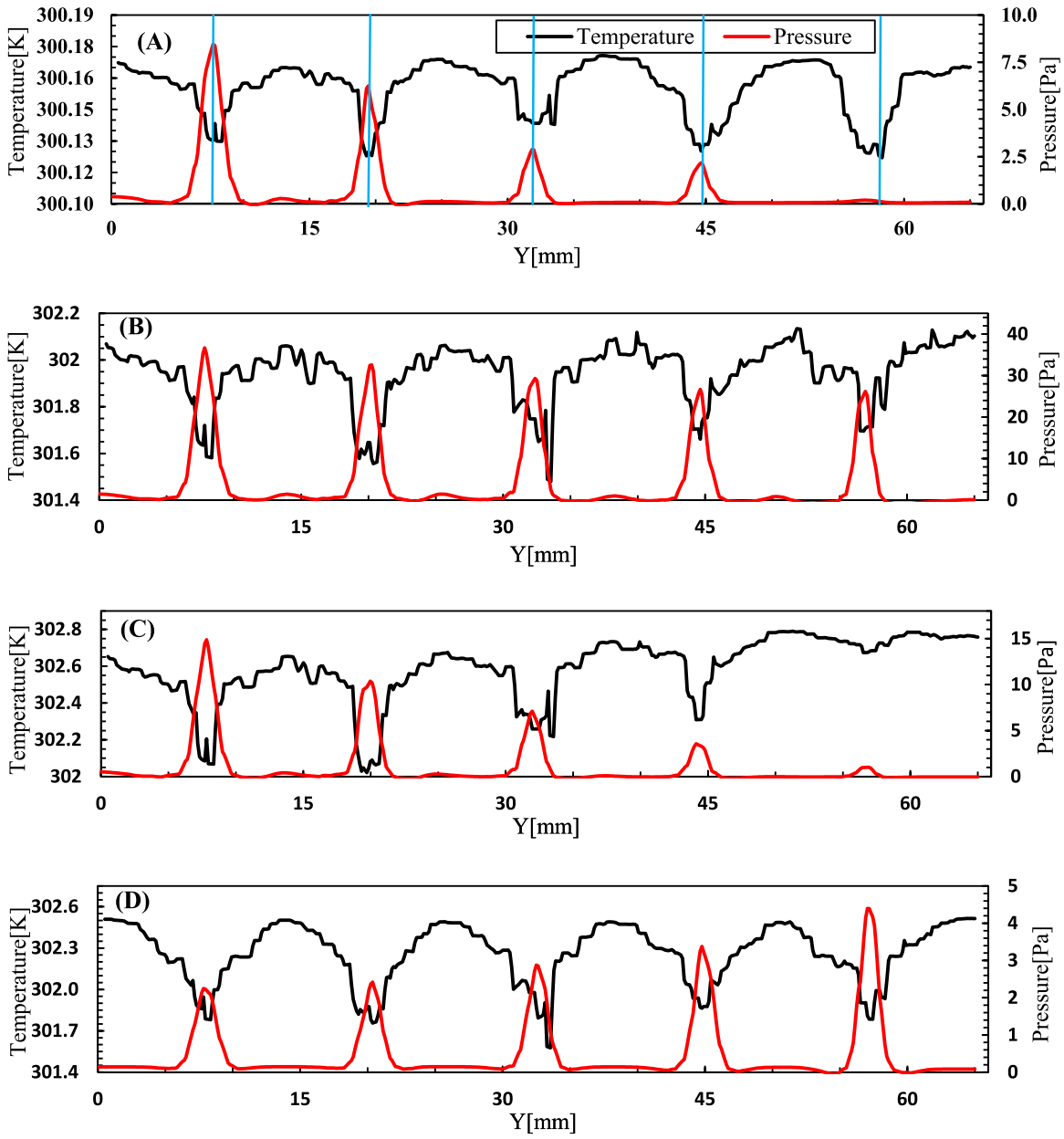

Fig. 11. Battery surface temperature variations in front of orifices, where designated in (A) with the simultaneous inlet air coolant pressure changes for the NYCC traffic drive cycle at the moments specified by A, B, C, and D in Fig. 10a.

during ramp 1. The maximum power demanded in WLTP is achieved through the ramp's inclination, which is 48 kW equivalent to 0.54C. However, this battery discharge rate is not crucial for the battery pack. If batteries operate with 20 % DoD at 0.54C, the temperature of the batteries rises to 301.5 K, and if batteries continue to be discharged to 100 % of DoD, the maximum temperature reaches 302 K at 0.54C.

Fig. 5b represents the Tehran driving cycle. The highest inclination and thus the highest power demand is 341 kW, which corresponds to 4C for each battery cell. By keeping the batteries at 4C, with 20 % DoD, the temperature can reach up to 308 K, and at 100 % DoD, the temperature reaches 325 K. As mentioned before, the optimum operating range for the batteries are somewhere between 288 and 308 K. Therefore, 100 Pa inlet air pressure of gauge is required for 20 % and 100 % DoD, which leads to a temperature drop to 303 K, and 307.5 K. That is to say, 12.85 % and 33.65 % temperature reductions are observed in 20 % and 100 % DoD, respectively. It should be noted that through this method, the temperature of the batteries can be evaluated only before and after the ramp, and the temperature evolutions during the ramp are not predicted. Given that the ramp duration is often very short, this omission remains acceptable.

5.1. Cooling performance on US06 driving cycle

The battery cooling performance during WLTP and Tehran driving cycles was evaluated using the first and second approaches (see Section 2.2.1). For the steepest ramp in WLTP, representing the maximum battery power requirement, the vehicle speed does not reach a large value. Hence, the batteries do not undergo a high discharge rate for an extended period. Other drive cycles were then employed to examine the second approach. Fig. 6 represents the US06 driving cycle and the power demand during the driving cycle, known as the high acceleration aggressive driving schedule or Supplemental Federal Test Procedure

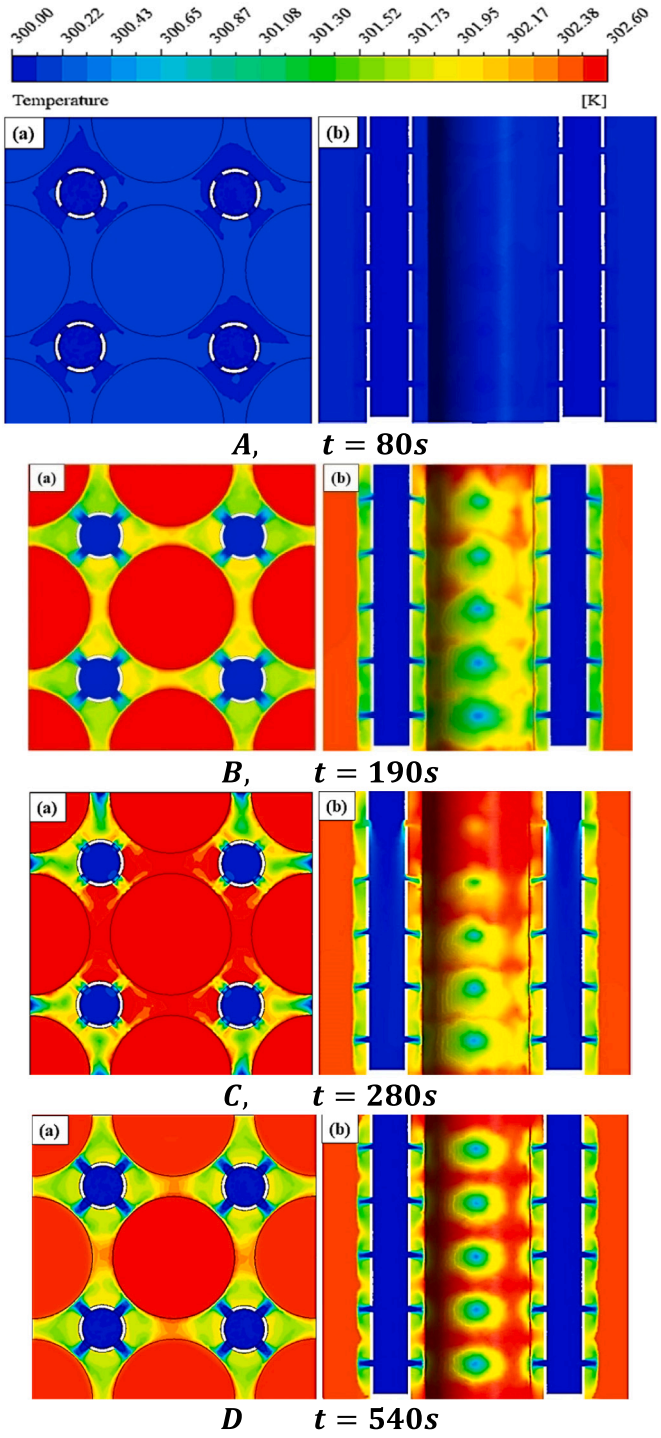

Fig. 12. The temperature variations contours by air-cooling for NYCC-traffic drive cycle (a) top view from cross section indicated in Fig. 1a (b) side view.

(SFTP) driving schedule. According to Fig. 6, the battery pack's temperature increases gradually over the first 300 s. This is because the US06 drive cycle represents aggressive city driving, and the first cycle in the series of three combined processes has a high discharge rate [70].

Here, based on the first approach, the maximum power is 170 kW from a high-velocity increase during the 585 to 600 s as shown in Fig. 6a, which is equivalent to 2C. Therefore, almost the maximum heat flux of the batteries is achieved, and the temperature rises to 302.5 K without cooling during this period. According to Fig. 6b, this temperature drops to 301.2 K by applying 0.0848 g/s of air coolant. It should be noted that the battery temperature could reach 313.5 K at the maximum DoD of 2C.

Based on the second approach (discussed in Section 2.2.1), the power time (Fig. 6a) is calculated from the velocity by converting every ascending ramp to mechanical power. Then, a transient simulation was carried out on the total driving cycle with cooling to assess the battery thermal performance throughout the driving cycle. The coolant pressure inlet varies during the US06 driving cycle by considering the dynamic cooling approach corresponding to heat flux generation based on Eq. (11). Fig. 6b shows the maximum temperature variation by using air cooling. A, B, C, and D are selected, as specific moments, to demonstrate the temperatures and changes at the inlet pressure of the coolant during the driving cycles. Furthermore, these quantities (Y(mm) in Fig. 1b) are shown for the selected moments. Due to the power variations during the driving cycles, the discharged current varies, resulting in an increase in the battery internal heat generation and a rise in the battery temperature [71].

Fig. 7 shows that for A, B, C, and D from Fig. 6a, the battery temperature significantly drops where the orifices are located (see Fig. 1). Each orifice issues a jet of coolant impinging on the surface of the battery, which highly enhances the cooling and reduces the battery temperature locally [48]. This arrangement further helps minimize the temperature difference along and between the battery cells.

Fig. 8 shows the temperature contours for different designated points on the US06 drive cycle. The selected areas of A, B, C, and D correspond to those in Fig. 6a, and the points are designated based on the thermal behaviors of the batteries throughout the US06 drive cycles.

Fig. 9 shows the fluid velocity contours at the times designated in Fig. 6a (A, B, C, and D) for the US06 driving cycle by air-cooling. Based on the velocity contours, the coolant's fluid velocity significantly increases between B, $t = 50$, and D, $t = 590$. This has resulted from the increase in vehicle velocity. As vehicle velocity increases, more power is required causing faster battery discharge. Thus, the temperature of the batteries increases (B and D), and dynamic cooling effects can be observed by enhancing inlet cooling fluid velocity.

5.2. Cooling performance on NYCC Traffic driving cycle

New York City Cycle (NYCC) driving cycle is specific to urban traffic mode, magnifying the required power. In this case, the vehicle may need to reach a high speed in a short period. This is different from the US06 driving cycle, pertinent to highway driving mode. Fig. 10a shows that with a lower maximum vehicle speed than the US06 driving cycle; the battery pack is exposed to a higher load. Based on the first approach, the maximum power requirement is 292 kW for a higher velocity ascend inclination, equivalent to 3.45C in the vehicle with a total battery pack capacity of 85 kW. The higher velocity ascends inclination is reached in 575–600 s (Fig. 10a), raising the temperature to 305 K without air-cooling. However, at 100 % DoD, 323 K is brought up by the current intensity corresponding to the 3.45C discharge rate. Although 305 K is within the safe range (below 308 K), and in this slope, the highest power is required from the battery pack, the temperature rise in the battery pack cannot be predicted accurately based on the first approach. This is because the first approach does not consider the temperature fluctuations during the driving cycle, especially in traffic mode. In the traffic mode, the maximum battery load is heavily related to the successive brakes and motion of the EVs.

The NYCC driving cycle diagram reveals that there are regions in which vehicles may be exposed to very high power levels, even if only for brief periods of 3 or 4 s for instance during the time period of 196–199.5 s in Fig. 10a. This highlights the need for further investigation into the impact of such high-power exposure on vehicle performance and the safety of the battery pack.

Based on the second approach (discussed in Section 2), the power-time figure (Fig. 10a) is achieved from the velocity-time by converting every ascending ramp to mechanical power (see Section 5.1). After 100 s

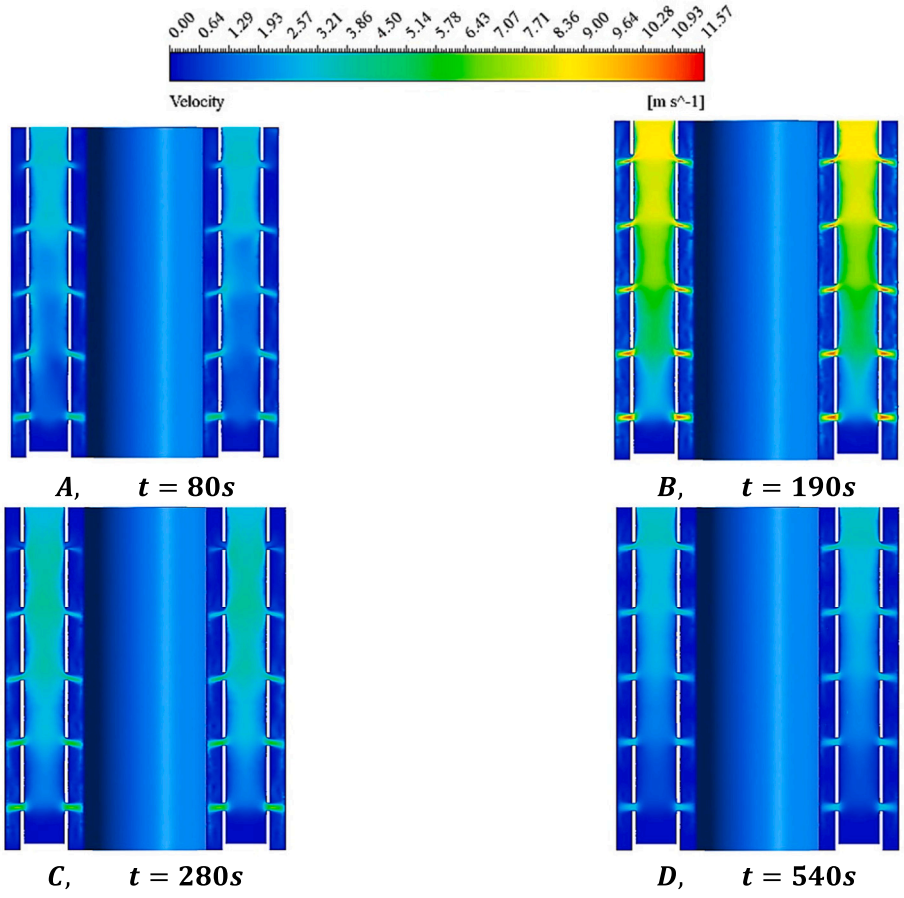

Fig. 13. The fluid velocity contours at A, B, C, and D in Fig. 10a by air-cooling in the NYCC traffic drive cycle.

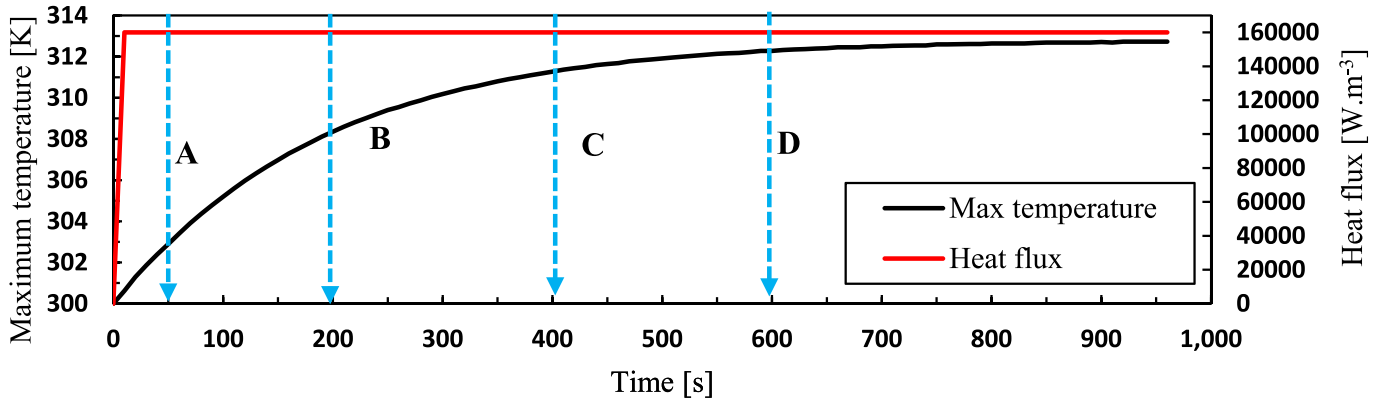

Fig. 14. The temperature and the heat flux variations in high-performance model with air-cooling.

in NYCC traffic mode, the power demand of the battery pack starts to increase, and accordingly, the temperature increases slightly (see Fig. 10b). However, after 240 s (see Fig. 10a) the maximum mechanical power is required until the EVs reaches the speed of 12 m/s, pushing the temperature to 302.8 K. In addition, A, B, C, and D are shown in Fig. 10a to depict the temperature and changes in the inlet coolant pressure at these moments in Fig. 11. The variations in the coolant pressure are similar to those in the US06 driving cycle. The temperature variations in different selected points are almost identical due to the dynamic cooling approach, which prevented batteries temperatures to exceed the safe range (308 K).

The red lines in Fig. 11, which represent the pressure changes along the battery length (Y(mm), show that where the orifices are located the pressure significantly increases. Hence, five peaks appear in the pressure changes in front of orifices in A, B, C, and D moments in Fig. 11, in which at B the pressure peaks are higher. Also, at B, the mechanical power reaches its maximum, causing a temperature rise in battery pack. Therefore, to keep the battery temperature within the safe region, the

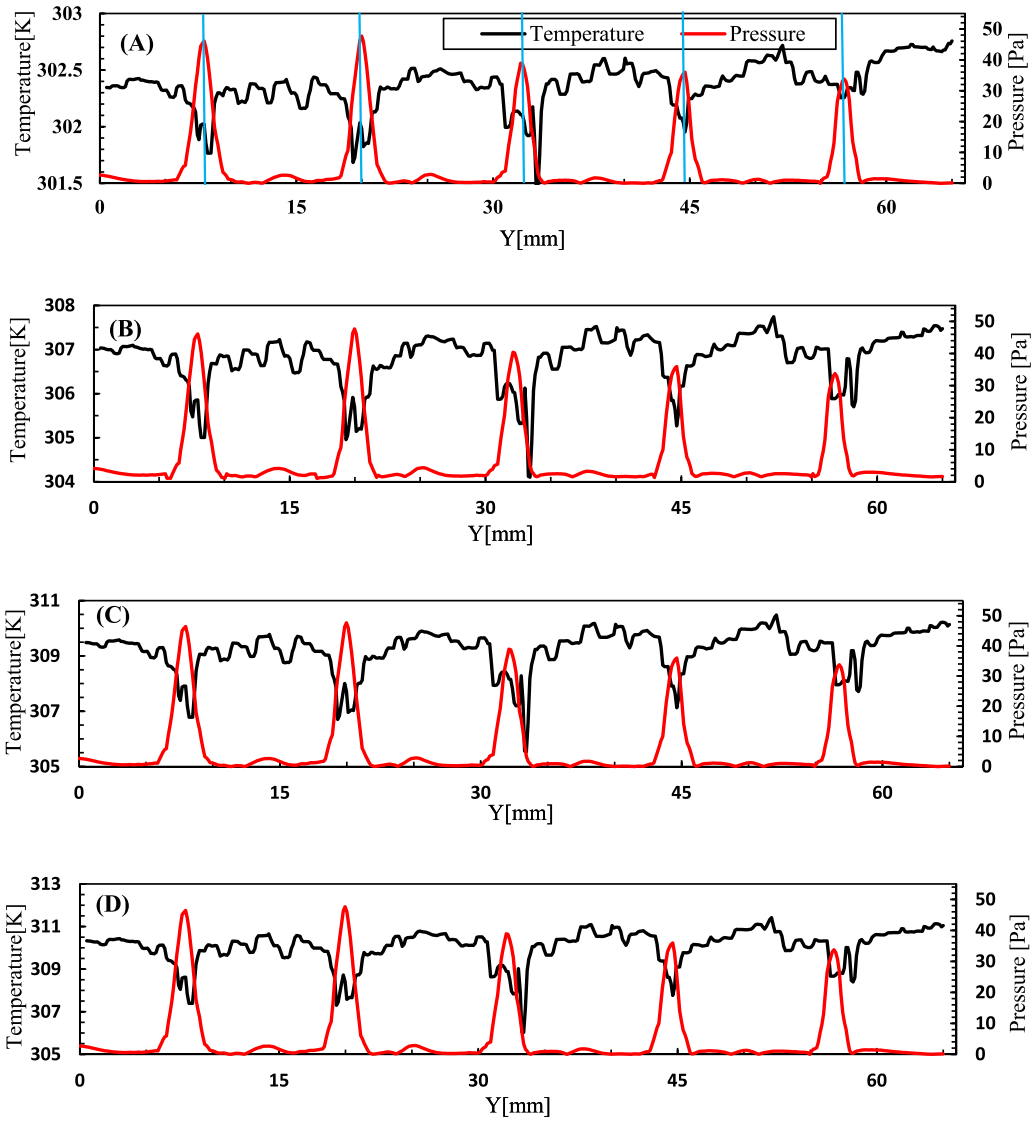

Fig. 15. Battery surface temperature variations in front of orifices, where designated in (A) for the high-performance model with constant inlet air coolant pressure at the moments specified by A, B, C, and D in Fig. 14.

inlet pressure (inlet pressure in Fig. 1a) also increases to near 100 Pa corresponding to 1.52 g/s. The pressure changes observed at the specified points indicate that dynamic cooling based on Eq. (11) works well, and it can be considered in battery thermal management as the optimal battery cooling.

Fig. 12 shows the temperature contours for different designated points on the NYCC traffic drive cycle. During the first 80s at A, the temperature of the batteries does not increase significantly, and the battery's temperature can be kept in a safe region. However, near the 190 s, the vehicle's velocity increases leading to a substantial power requirement and an increase in the battery's temperature. Albeit, based on the dynamic cooling system, the inlet pressure increases as well.

In the NYCC traffic driving cycle, the battery temperature remains within the safe region. Therefore, as Fig. 13 shows, the fluctuations in the coolant inlet velocity are negligible, except for that at B, $t = 190s$. The fluid velocity increases at this moment of time because of the power increment and the subsequent increase in the current withdrawal from the batteries. Hence the temperature of the batteries rises resulting in increasing the coolant flow rate. This process is similar to that in the UC06 driving cycle at B, $t = 50$, and D, $t = 590$ shown in Fig. 9.

5.3. High-performance mode, air

In the current investigation, a battery pack with a capacity of 85 kW is evaluated, with the capability to reach 60 miles per hour in 3.1 s in some vehicles. To achieve this, the 517 kW mechanical power is required from the batteries in a limited time of 3.1 s [46], leading to a 6C discharge rate. Moreover, the heat flux equation is calculated based on the production of this current intensity. Hence, according to Fig. 14, the heat flux can sharply increase and reach nearly 160 $kW.m^{-3}$, after the 517 kW power extraction from the battery pack in 3.1 s. However, the batteries maximum temperature, slowly increased. This is because of the solid-electrolyte interphase layer and internal resistance in heat transfer. In the current investigation, the battery discharge rate after 3.1 s was not stopped to allow for assessing the maximum temperature rise at 100 % DoD at a 6C rate. Therefore, the shock of instantaneous power extractions is extended throughout the 900 s. It is important to note that no vehicle can operate in this condition due to speed limitations and the presented results correspond to the dynamometer condition [72]. The maximum temperature of the batteries reached 335 K after 100 % DoD at 6C and the maximum temperature is 55.67 % higher than the safe range of 308 K. According to Fig. 14, under air-cooling, the maximum

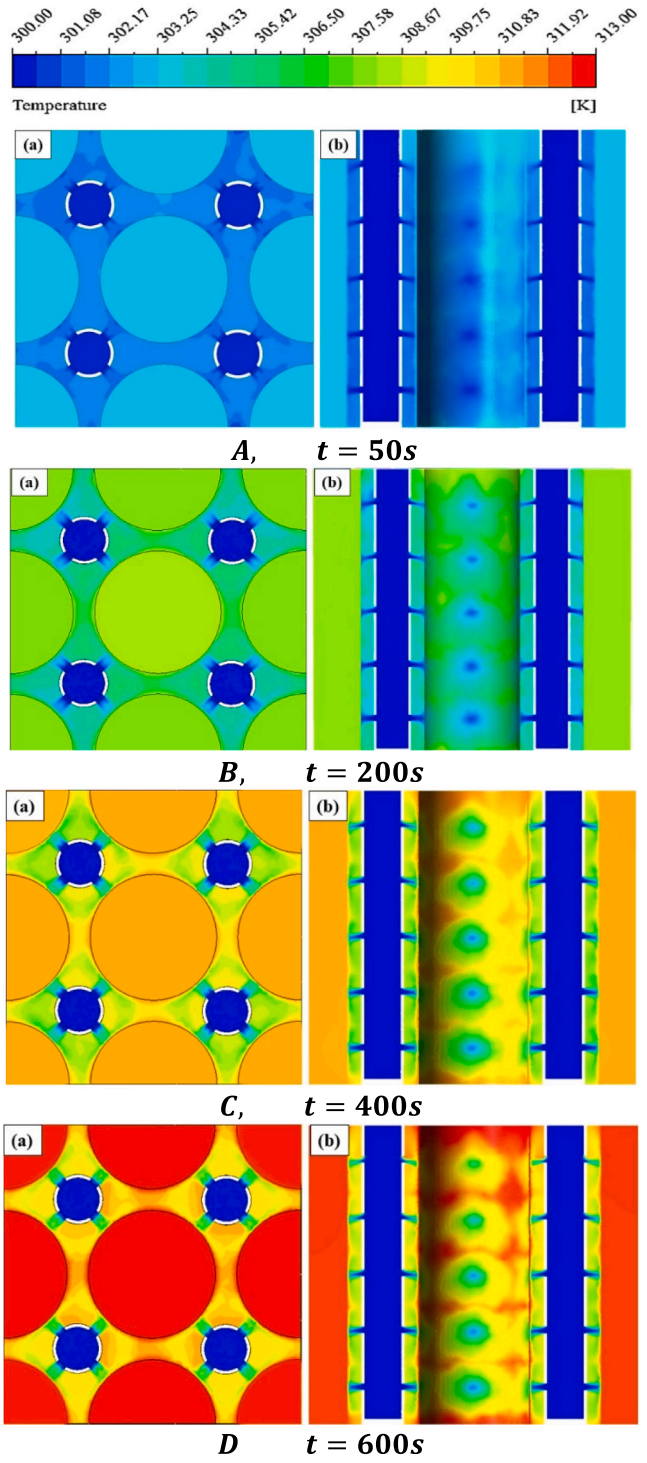

Fig. 16. The temperature variations contours through the air coolant for the high-performance mode (a) top view from cross section indicated in Fig. 1a (b) side view.

temperature is 312 K. In addition, the maximum air-cooling pressure inlet does not exceed 150 Pa (equivalent to the maximum 2.71 g/s mass flow rate). Accordingly, after 200 s, the batteries temperature exceeds the critical value of 308 K, and practically the air cooling system cannot keep the temperature of the battery low enough [48]. However, after 600 s, the batteries temperature with the use of air-cooling declined by 45.54 % compared to their maximum temperature. Of course, liquid cooling can be used as an efficient cooling in high-performance driving cycles, as demonstrated in Fig. 1 in Supplementary Materials, this figure shows water-based transient cooling for the high-performance mode.

Fig. 15 shows that the inlet pressure through the orifices is almost identical for the A, B, C, and D. At the same time, the temperature variations in these moments significantly vary because of maintaining the battery heat flux and power extraction during the 950 s period. In Fig. 15, the temperature fluctuations along the batteries (Y(mm) indicated in Fig. 1b) at A, B, C, and D increase, respectively. This behavior can be also seen in Fig. 14 by increasing the maximum battery temperature over 900 s.

Fig. 16 demonstrates the temperature contours for different designated points on the high-performance model. The temperatures increase during the process in different selected moments. Importantly, in the $t = 400s$ and $t = 600s$, the temperature of the batteries exceeds the safe limit, and the necessity of using another cooling fluid is quite evident in these time steps, as discussed later.

Fig. 17 illustrates the velocity distributions of air flow at A, B, C, and D for the high-performance mode. For all the investigated moments of time, the air inlet pressure and flow rate are 150 Pa and 2.71 $\frac{g}{s}$, respectively. This is due to keeping the EV's power demand steady at its maximum value for over 950 s. In addition, during this process, the maximum current withdrawal from the batteries makes the battery temperature rise.

The summary of cooling methodology based on a different approach for different driving cycles can be found in Table 1 of Supplementary Materials.

5.4. Nusselt number

Fig. 18 represents the Nusselt number changes along the battery cell for different driving cycles over A, B, C, and D. The Nusselt number is calculated for various modes, including liquid and air selected for the high-performance mode, New York City Cycle traffic mode by air-cooling, and US06 by air-cooling. As the speed of EV's increases, the fluid inlet pressure increases (see Eq. (11)), and the inlet pressure is directly related to the temperature variations of the battery cell. Further, higher flow velocities enhance the convective heat transfer. Hence, the heat transfer rate and Nusselt number are improved in EV accelerated movements like the points B and D in Fig. 18c and A in Fig. 8d.

According to Fig. 18, to calculate the Nusselt number, a line is considered on the battery surface, and in front of the orifices, from top to bottom (see Fig. 1b). The Nusselt number is calculated along this line. The observed fluctuations along the battery length with several peaks on the y-axis (along the battery surface) correspond to peak values where the jets issued from the orifices impinges upon the battery surface [48]. Therefore, by increasing the fluid pressure through the orifices, the convective heat transfer coefficient improves, indicated by the higher values of the Nusselt number.

The Nusselt numbers in lower orifices (see Fig. 1b) are larger compared to those for the orifices positioned at the top of the batteries. As already discussed, for air-cooling, there exists some pressure difference between the pipes' top and bottom, and the pressure at the bottom of the distribution pipe is higher. However, this is not the case in water cooling. Hence, in Fig. 18b, because of the higher fluid pressure at the top of the distribution pipes, the water velocities are higher through the orifices positioned at the top of the battery (Fig. 1b), leading to the Nusselt numbers being higher at the top of the battery.

Fig. 18 also shows the differences between the Nusselt number at A, B, C, and D for different driving cycles. For instance, in the high-performance mode in both air and water coolant, the differences are relatively negligible among A, B, C, and D. This is due to the pressure inlet (Fig. 1a) being approximately constant during the driving cycles. However, the differences between the specified moments in NYCC traffic air-cooled and US06 air-cooled (Fig. 18c and d) are quite noticeable. In

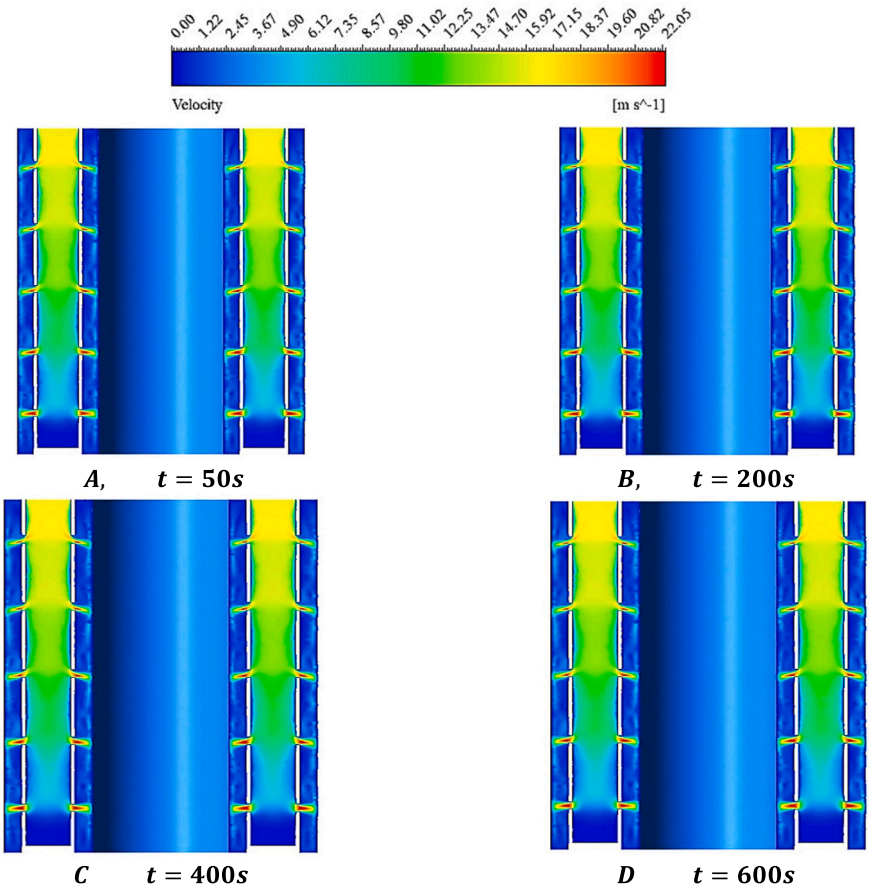

Fig. 17. The fluid velocity contours at the moments specified by A, B, C, and D in Fig. 14 through air cooling in the high-performance mode.

Fig. 18c, for B, the fluid inlet velocity significantly increases due to the enhancement in power requirement (see Fig. 10a), and the Nusselt number increases as well. To a lesser extent, the same behavior is observed at D. Furthermore, in Fig. 18d, for A, the required power is relatively higher than that in other moments (B, C, and D) Fig. 6a shows. Therefore, the battery temperature increment is also higher than other moments, which increases the air inlet velocity and subsequently the Nusselt number.

6. Conclusions

Time-dependent, battery thermal management under the load applied by a few standard driving cycles was examined numerically. In the investigated dynamic cooling, the fluid inlet velocity varied based on the battery discharge rate. The key results are summarized in the following.

- In the US06 driving cycle, based on the first approach, the maximum power was 170 kW from a high velocity increase during this cycle, equivalent to 2C. In this state, the temperature of the batteries reached 313.5 K in 100 % DoD.
- The battery temperature significantly drops where the orifices are located. Each orifice issues a jet of coolant impinging on the surface of the battery, which highly enhances cooling and thus reduces the battery temperature locally.
- For the NYCC-traffic driving cycle, the maximum power requirement reached 292 kW from a high velocity increase based on the first approach, which is equivalent to 3.45 C. In this state, the temperature of the batteries increases to 305.5 K during the 575–600 s in the driving cycle.
- In high-performance mode, the maximum temperature of the batteries reached 335 K for 100 % DoD at a 6C discharge rate. For 2.71 g/s inlet mass flow rate, the battery temperature drops to 312 K.
- In the high-performance model with the air-cooling, the temperature of the batteries exceeds the safe limit, unless 2.71 g/s of coolant is pumped through the system.
- In the high-performance cycle and for liquid cooling, the battery temperature reaches 304 K with a 31 K temperature reduction compared to air-cooling.
- The Nusselt number is higher at the bottom of the batteries positioned in front of the orifices compared to the top in air-cooling. However, the opposite behavior is observed in liquid cooling. This is due to the pressure differences between the top and bottom of the system set by the viscosity differences of the coolants.
- The Nusselt number in NYCC traffic and US06 air-cooled varies for different specified moments. This is because in accelerated movements where the power withdrawal increases, the inlet coolant fluid pressure is also increased leading to higher values of the Nusselt number.

This investigation demonstrated the importance of considering unsteady effects in the design of battery thermal management systems in electric vehicles based on different driving cycles. The two electrochemical-thermal modeling methods based on power withdrawal during the driving cycles are flexible and can be implemented in any three-dimensional battery structure. Future research can focus on optimizing the structure of the batteries and fluid flow to reduce weight and improve cooling efficiency. It is important to highlight that the methodologies utilized in this study are not limited to the specific Lithium-ion battery type under investigation. These techniques can be used in any

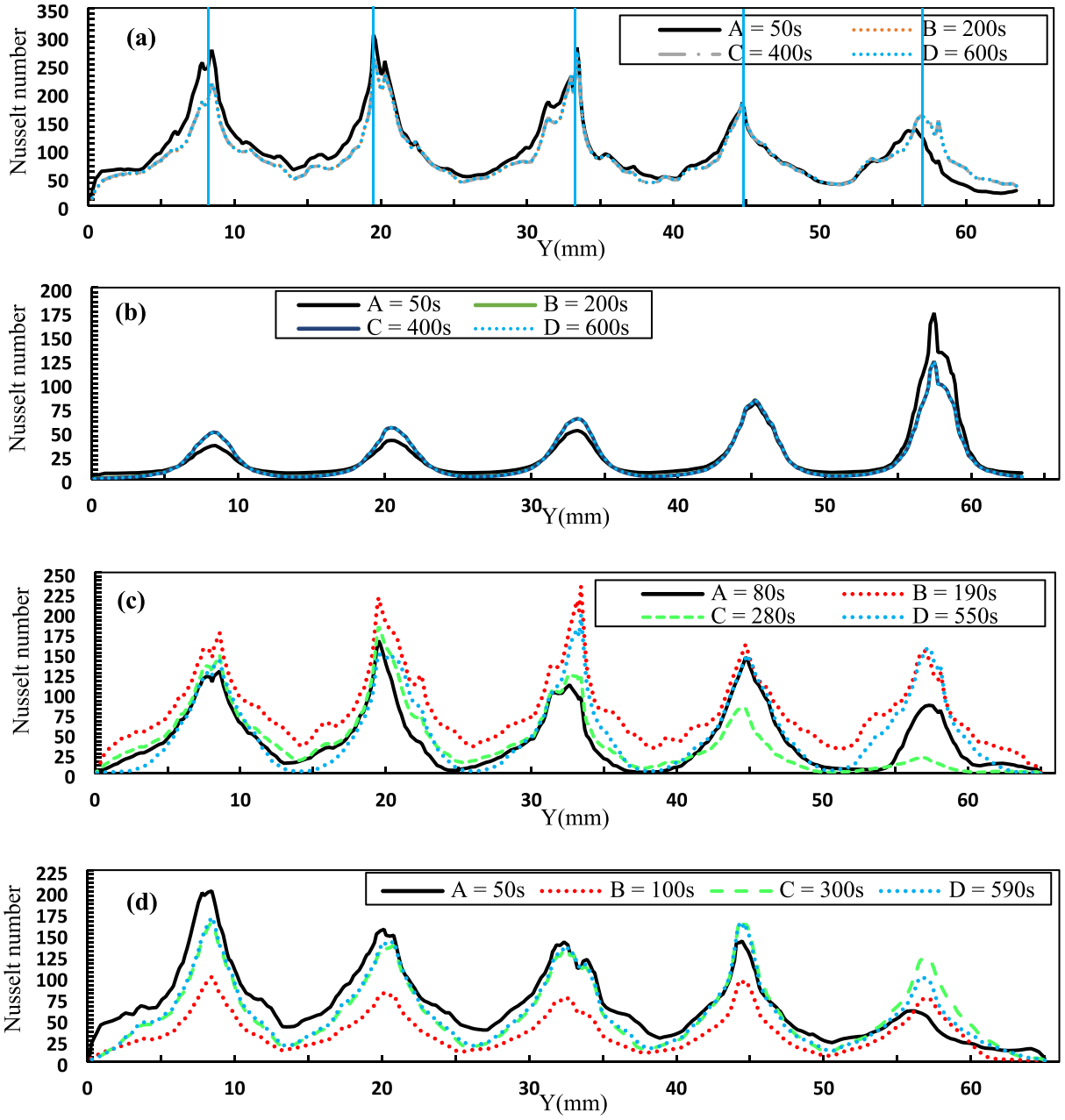

Fig. 18. Nusselt variations along the battery length at A, B, C, and D for (a) high-performance mode air-cooled, and vertical line indicated orifices locations (b) high-performance water cooled (c) NYCC traffic air-cooled, and (d) US06 air-cooled.

future research for other types of Lithium-ion batteries. Additionally, the impact of ambient conditions on the battery's thermal behavior can be studied in different urban driving cycles.

CRediT authorship contribution statement

Jalal Jahanpanah: Writing (original draft, Review & Editing), Methodology, Investigation, Data Curation, Visualization.

Peyman Soleymani: Writing (original draft, Review & Editing), Methodology, Investigation, Data Curation, Visualization.

Nader Karimi: Writing (Review & Editing), Supervision, Methodology, Conceptualization.

Meisam Babaie: Writing (Review & Editing), Supervision, Methodology.

Seifolah Saedodin: Supervision.

Declaration of competing interest

The authors declare that they have no known competing financial interests or personal relationships that could have appeared to influence the work reported in this paper.

Data availability

No data was used for the research described in the article.

Appendix A. Supplementary data

Supplementary data to this article can be found online at https://doi.org/10.1016/j.est.2023.109278.

References

[1] International Energy Agency (IEA), World energy outlook. https://www.iea.org/reports/world-energy-outlook-2010.
[2] M. Tran, et al., Realizing the electric-vehicle revolution, Nat. Clim. Chang. 2 (5) (2012) 328–333.
[3] P. Soleymani, et al., Experimental investigation of a hybridized flat-plate solar collector/gas burner for low-carbon production of hot water–analysis of energy, exergy, and GHG emissions, Sustainable Energy Technol. Assess. 55 (2023), 102918.
[4] C. Chen, et al., Robust planning of energy and environment systems through introducing traffic sector with cost minimization and emissions abatement under multiple uncertainties, Appl. Sci. 9 (5) (2019) 928.
[5] A.R. Bhatti, et al., A comprehensive overview of electric vehicle charging using renewable energy, Int. J. Power Electron. Drive Syst. 7 (1) (2016) 114.
[6] X. Yin, Z. Jiang, A novel continuously variable-speed offshore wind turbine with magnetorheological transmission for optimal power extraction, Energy Sources, Part A 45 (3) (2023) 6869–6884.
[7] X. Yin, Z. Jiang, M. Lei, Quantifying the effects of high-speed shaft braking on the substructural dynamics of monopile offshore wind turbines, Energy Sources Part A 44 (4) (2022) 9779–9795.
[8] J. Wang, et al., Optimal design of combined operations of wind power-pumped storage-hydrogen energy storage based on deep learning, Electr. Pow. Syst. Res. 218 (2023), 109216.
[9] X. Yin, M. Lei, Jointly improving energy efficiency and smoothing power oscillations of integrated offshore wind and photovoltaic power: a deep reinforcement learning approach, Prot. Control Mod. Power Syst. 8 (1) (2023) 25.
[10] X. Yin, Z. Zhao, W. Yang, Predictive operations of marine pumped hydro-storage towards real time offshore wind-wave power complementarity: an event-triggered MPC approach, J. Energy Storage 62 (2023), 106583.
[11] Y. Ye, et al., Numerical analyses on optimizing a heat pipe thermal management system for lithium-ion batteries during fast charging, Appl. Therm. Eng. 86 (2015) 281–291.
[12] M.S. Patil, et al., Cooling performance characteristics of 20 Ah lithium-ion pouch cell with cold plates along both surfaces, Energies 11 (10) (2018) 2550.
[13] X. Yin, W. Yang, J. Yang, Influence of emergency mechanical braking on the supporting platform performances of floating offshore wind turbines, Ocean Eng. 266 (2022), 112010.
[14] A.A. Pesaran, Battery thermal models for hybrid vehicle simulations, J. Power Sources 110 (2) (2002) 377–382.
[15] Q.B. Li, C.B. Yang, S. Santhanagopalan, K. Smith, J. Lamb, L.A. Steele, et al., Numerical investigation of thermal runaway mitigation through a passive thermal management system, J. Power Sources 429 (2019) 80–88.
[16] S. Liu, et al., Experimental and simulation study on thermal characteristics of 18,650 lithium–iron–phosphate battery with and without spot–welding tabs, Appl. Therm. Eng. 166 (2020), 114648.
[17] J. Xun, R. Liu, K. Jiao, Numerical and analytical modeling of lithium ion battery thermal behaviors with different cooling designs, J. Power Sources 233 (2013) 47–61.
[18] U.S. Kim, et al., Modelling the thermal behaviour of a lithium-ion battery during charge, J. Power Sources 196 (11) (2011) 5115–5121.
[19] Z. Rao, S. Wang, Y. Zhang, Simulation of heat dissipation with phase change material for cylindrical power battery, J. Energy Inst. 85 (1) (2012) 38–43.
[20] Z. Rao, et al., Experimental investigation on thermal management of electric vehicle battery with heat pipe, Energ. Conver. Manage. 65 (2013) 92–97.
[21] L. Tran, et al., Li-ion battery cooling system integrates in nano-fluid environment, Appl. Nanosci. 7 (1) (2017) 25–29.
[22] K. Somasundaram, E. Birgersson, A.S. Mujumdar, Thermal–electrochemical model for passive thermal management of a spiral-wound lithium-ion battery, J. Power Sources 203 (2012) 84–96.
[23] D.K. Sharma, A. Prabhakar, A review on air cooled and air centric hybrid thermal management techniques for Li-ion battery packs in electric vehicles, J.Energy Storage 41 (2021), 102885.
[24] N. Akkurt, et al., Cooling of non-sloped, positively sloped, and negatively sloped arrangements of Li-ion batteries with a phase change material connected to a solar system, J. Energy Storage 52 (2022), 104808.
[25] S. Rashidi, et al., Progress and challenges on the thermal management of electrochemical energy conversion and storage technologies: fuel cells, electrolysers, and supercapacitors, Prog. Energy Combust. Sci. 88 (2022), 100966.
[26] S. Park, D. Jung, Battery cell arrangement and heat transfer fluid effects on the parasitic power consumption and the cell temperature distribution in a hybrid electric vehicle, J. Power Sources 227 (2013) 191–198.
[27] M. Akbarzadeh, et al., A novel liquid cooling plate concept for thermal management of lithium-ion batteries in electric vehicles, Energ. Conver. Manage. 231 (2021), 113862.
[28] L. Saw, A. Tay, L.W. Zhang, Thermal management of lithium-ion battery pack with liquid cooling, in: 2015 31st Thermal Measurement, Modeling & Management Symposium (SEMI-THERM), IEEE, 2015.
[29] H. Behi, et al., Aluminum heat sink assisted air-cooling thermal management system for high current applications in electric vehicles, in: 2020 AEIT International Conference of Electrical and Electronic Technologies for Automotive (AEIT AUTOMOTIVE), IEEE, 2020.
[30] A.K. Thakur, et al., A state of art review and future viewpoint on advance cooling techniques for Lithium–ion battery system of electric vehicles, J. Energy Storage 32 (2020), 101771.
[31] J. Kim, J. Oh, H. Lee, Review on battery thermal management system for electric vehicles, Appl. Therm. Eng. 149 (2019) 192–212.
[32] Y. Deng, et al., Effects of different coolants and cooling strategies on the cooling performance of the power lithium ion battery system: a review, Appl. Therm. Eng. 142 (2018) 10–29.
[33] H. Sun, R. Dixon, Development of cooling strategy for an air cooled lithium-ion battery pack, J. Power Sources 272 (2014) 404–414.
[34] S. Basu, et al., Coupled electrochemical thermal modelling of a novel Li-ion battery pack thermal management system, Appl. Energy 181 (2016) 1–13.
[35] H. Wang, F. He, L. Ma, Experimental and modeling study of controller-based thermal management of battery modules under dynamic loads, Int. J. Heat Mass Transf. 103 (2016) 154–164.
[36] Z. Ling, et al., A hybrid thermal management system for lithium ion batteries combining phase change materials with forced-air cooling, Appl. Energy 148 (2015) 403–409.
[37] D. Ouyang, et al., A review on the thermal hazards of the lithium-ion battery and the corresponding countermeasures, Appl. Sci. 9 (12) (2019) 2483.
[38] L. Yiding, et al., A safety performance estimation model of lithium-ion batteries for electric vehicles under dynamic compression, Energy 215 (2021), 119050.
[39] X. Yu, et al., Experimental study on transient thermal characteristics of stagger-arranged lithium-ion battery pack with air cooling strategy, Int. J. Heat Mass Transf. 143 (2019), 118576.
[40] C.G. Motloch, et al., High-power battery testing procedures and analytical methodologies for HEV's, SAE Trans. (2002) 797–802.
[41] A. Saeed, N. Karimi, M.C. Paul, Analysis of the unsteady thermal response of a Li-ion battery pack to dynamic loads, Energy 231 (2021), 120947.
[42] A. Saeed, N. Karimi, M.C. Paul, Computational assessment of the thermal response of a Li-ion battery module to transient loads, J. Power Sources 552 (2022), 232217.
[43] S. Chacko, Y.M. Chung, Thermal modelling of Li-ion polymer battery for electric vehicle drive cycles, J. Power Sources 213 (2012) 296–303.
[44] K. Darcovich, et al., Coupled electrochemical and thermal battery models for thermal management of prismatic automotive cells, Appl. Therm. Eng. 133 (2018) 566–575.
[45] K. Monika, S.P. Datta, Comparative assessment among several channel designs with constant volume for cooling of pouch-type battery module, Energ. Conver. Manage. 251 (2022), 114936.
[46] Tesla Model, S, Specifications and Features, 2012.
[47] https://www.tesla.com/sites/default/files/tesla-model-s.pdf.
[48] H. Zhou, et al., Thermal performance of cylindrical Lithium-ion battery thermal management system based on air distribution pipe, Int. J. Heat Mass Transf. 131 (2019) 984–998.
[49] ANSYS Inc, Help System. Theory Guide, A.F.R, 2018.
[50] G.-H. Kim, et al., Multi-domain modeling of lithium-ion batteries encompassing multi-physics in varied length scales, J. Electrochem. Soc. 158 (8) (2011) A955.
[51] M. Doyle, T.F. Fuller, J. Newman, Modeling of galvanostatic charge and discharge of the lithium/polymer/insertion cell, J. Electrochem. Soc. 140 (6) (1993) 1526.
[52] K. Smith, C.-Y. Wang, Power and thermal characterization of a lithium-ion battery pack for hybrid-electric vehicles, J. Power Sources 160 (1) (2006) 662–673.
[53] K. Kumaresan, G. Sikha, R.E. White, Thermal model for a Li-ion cell, J. Electrochem. Soc. 155 (2) (2007) A164.
[54] A. Jokar, et al., Review of simplified Pseudo-two-dimensional models of lithium-ion batteries, J. Power Sources 327 (2016) 44–55.
[55] H. Zhang, et al., Thermal analysis of a 6s4p Lithium-ion battery pack cooled by cold plates based on a multi-domain modeling framework, Appl. Therm. Eng. 173 (2020), 115216.
[56] M.-K. Tran, et al., Effect of integrating the hysteresis component to the equivalent circuit model of Lithium-ion battery for dynamic and non-dynamic applications, J. Energy Storage 32 (2020), 101785.
[57] M.S. Patil, J.-H. Seo, M.-Y. Lee, A novel dielectric fluid immersion cooling technology for Li-ion battery thermal management, Energ. Conver. Manage. 229 (2021), 113715.
[58] B. Saha, et al., An integrated approach to battery health monitoring using Bayesian regression and state estimation, in: 2007 IEEE Autotestcon, Ieee, 2007.
[59] B. Saha, et al., Prognostics methods for battery health monitoring using a Bayesian framework, IEEE Trans. Instrum. Meas. 58 (2) (2008) 291–296.
[60] B. Saha, K. Goebel, Uncertainty management for diagnostics and prognostics of batteries using Bayesian techniques, in: 2008 IEEE Aerospace Conference, IEEE, 2008.
[61] M. Pourramezan, H. Ajam, Modeling for thermal augmentation of turbulent flow in a circular tube fitted with twisted conical strip inserts, Appl. Therm. Eng. 105 (2016) 509–518.
[62] F. Moukalled, et al., The Finite Volume Method, Springer, 2016.
[63] S. Patankar, Numerical Heat Transfer and Fluid Flow, Taylor & Francis, 2018.
[64] S. Heinz, Remarks on energy partitioning control in the PITM hybrid RANS/LES method for the simulation of turbulent flows, Flow Turbul. Combust. 108 (4) (2022) 927–933.
[65] T.-H. Shih, et al., A new k-ϵ eddy viscosity model for high Reynolds number turbulent flows, Comput. Fluids 24 (3) (1995) 227–238.
[66] P. Soleymani, et al., Numerical investigation on turbulent flow, heat transfer, and entropy generation of water-based magnetic nanofluid flow in a tube with hemisphere porous under a uniform magnetic field, Int. Commun. Heat Mass Transfer 137 (2022), 106308.
[67] H. Liu, E. Chika, J. Zhao, Investigation into the effectiveness of nanofluids on the mini-channel thermal management for high power lithium ion battery, Appl. Therm. Eng. 142 (2018) 511–523.

[68] S. Li, et al., Optimal cell tab design and cooling strategy for cylindrical lithium-ion batteries, J. Power Sources 492 (2021), 229594.
[69] S.B. Peterson, J. Apt, J. Whitacre, Lithium-ion battery cell degradation resulting from realistic vehicle and vehicle-to-grid utilization, J. Power Sources 195 (8) (2010) 2385–2392.
[70] M. Malik, et al., Thermal and electrical performance evaluations of series connected Li-ion batteries in a pack with liquid cooling, Appl. Therm. Eng. 129 (2018) 472–481.
[71] K. Darcovich, et al., Comparison of cooling plate configurations for automotive battery pack thermal management, Appl. Therm. Eng. 155 (2019) 185–195.
[72] S. Sato, et al., Experimental driving performance evaluation of battery-powered medium and heavy duty all-electric vehicles, Int. J. Electr. Power Energy Syst. 141 (2022), 108100.